A proposal of building new muon small wheels : the NSW project

Draft 0.00 24.08.2011

Abstract

abstract

1 Introduction [TK]

The physics goal of the LHC includes among others discovery of Higgs boson, SUSY particles if they exist and other possible heavy particles which have not been explored at lower energy colliders. Once discovered the nature of what have been discovered should be studied in detail, and much data will be needed for it. Large integrated luminosity also allows access to rarer processes and higher centre-of-mass energies of colliding partons. Hence there is a plan of LHC upgrade by increasing its luminosity beyond the design value allowing for collecting much higher integrated luminosity than initially considered.

The upgrade will proceed in several steps. After the shutdown in 2013/14, the beam energy will increase to close to 7 TeV, and the luminosity will reach the nominal value $1 \times 10^{34}\mathrm{cm}^{-2}\mathrm{s}^{-1}$. Then after the second long shutdown in 2018, luminosity will be further increased to 2-$3 \times 10^{34}\mathrm{cm}^{-2}\mathrm{s}^{-1}$. The last step is to make significant changes to the IP region so that the luminosity is ramped up to $5 \times 10^{34}\mathrm{cm}^{-2}\mathrm{s}^{-1}$ with luminosity levelling aiming for collecting a total of 3000 fb^{-1} in the following 10 years.

In order to benefit from the high luminosity operation of the LHC, performance of the ATLAS detector should be maintained or even improved compared to the present performance at lower luminosity. In order to prepare for the LHC upgrade, we have been studying necessary changes to the muon spectrometer. Particularly important are the following two issues.

- Rate of level-1 muon trigger will naturally increase proportional to instantaneous luminosity. However there is a limitation on the total L1 rate. Raising the p_T threshold will leads to a loss of physics acceptance for many physics channels. Sharpening of the p_T threshold should therefore be considered as a means to control the L1 rate. This include improvement of p_T resolution and reduction of background.
- Due to the increase of cavern background rate, performance of the tracking chambers, both MDTs and CSCs, will degrade. Particular concern is in the muon EI station which is located close to the beam line and it is the region of highest cavern background.

We propose to build a pair of new small wheel detector (NSW) to replace the existing ones during the second long shutdown in order to be prepared to the LHC running with luminosity beyond the design value. The goal of NSW is to bring a significant enhancement of the muon performance in the endcap region, in particular of the level-1 muon trigger as well as the precision muon tracking, that would not be achieved by simple modifications alone such as improvement of radiation shielding or upgrade of electronics.

In the following sections, we discuss the detail of the proposal. The two main motivations, L1 upgrade and tracking upgrade, are discussed in detail in section 2. Requirements on the NSW are summarised in section xxx. To realise the requirements, there are three proposed technologies of detector and electronics. They are discussed in sections x,y and z. In section www, we discuss the expected muon performance with NSW. Finally a summary of cost, resources and schedule are given in section zzz.

2 Upgrade motivations [TK]

The muon small wheel is the first station (the inner station: EI) in the endcap of the ATLAS muon spectrometer (Figure 1). Together with the middle (EM) and outer (EO) stations, it provides the space coordinates (local track segments) for the reconstruction of charged particle tracks. Between the small wheel and the EM station a toroidal magnet is located with a bending power ranging from 3 to 7 Tm, depending on η and ϕ, allowing a determination of the momentum with high accuracy.

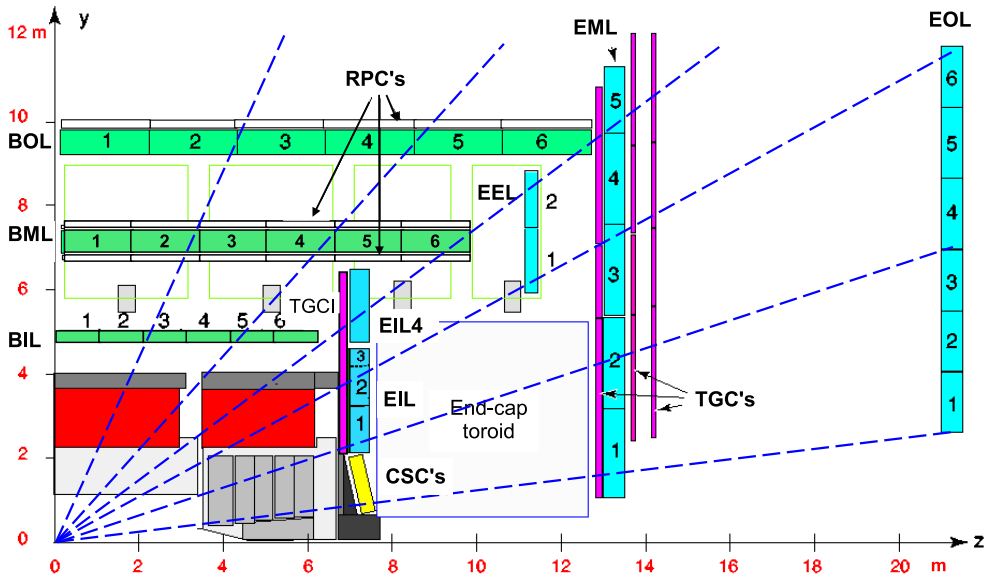

Figure 1: A z-y view of 1/4 of the ATLAS detector. The blue boxes indicate the endcap MDT chambers and the yellow box CSC.

The small wheel detector consists of 4+4 layers of monitored drift tube (MDT) chambers for precision tracking in the bending direction. Azimuthal coordinates are measured by two layers of thin gap chambers (TGC). These detectors cover the η range of $1.3 < |\eta| < 2.0$. The inner part of the small wheel is instrumented by four layers of cathode readout chambers (CSC) because of its higher rate capability. Each CSC layers determines both bending and azimuthal coordinates. The coverage of the CSC chambers is $2.0 < |\eta| < 2.7$. The chambers are arranged in 16 overlapping azimuthal sectors of alternating large-small sectors (Figure 2).

The middle station (EM) consists of MDT chambers for precision coordinates in the bending direction, and TGC chambers for level-1 muon trigger in the endcap. TGCs also provide azimuthal coordinates of the EM track segments. The EO station on the other hand consists only of MDT chambers.

2.1 Cavern background and tracking chambers

Cavern background, MDT efficiency vs rate, MDT occupance vs rate, CSC efficinecy vs rate,

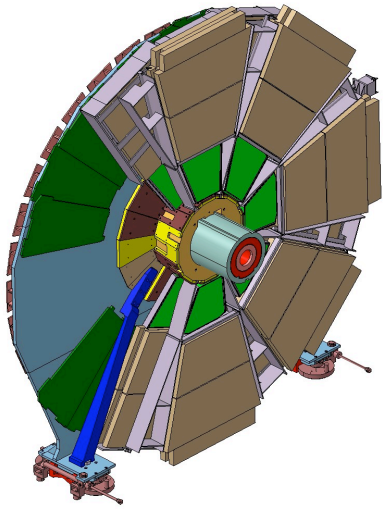

Figure 2: Structure of the present small wheel.

....

Since the small wheels are located at close to the beam line, it is the place of the highest counting rate in the muon spectrometer. A large fraction of hits are due to low energy photons and neutrons originating from particles created by beam collisions and escaped from absorption in the radiation shielding around the beam pipe and calorimeter materials. Such particles are generically referred to as 'cavern background'.

The rate of cavern background will increase proportionally to the beam luminosity. The muon spectrometer was designed to sustain at the rate expected for the nominal LHC luminosity of $1 \times 10^3 4\text{cm}^{-2}\text{s}^{-1}$ including the safety factor 5 which reflects the uncertainty on the estimation of hits due to cavern background.

Single tube efficinecy of MDT decreases almost linearly to the average tube rate as shown in Figure 3. With a diameter of 30 mm and tube length of xx - xx cm, MDT tubes see hit rate of xx - xx Hz/tube, according to the above estimation, in the inner most MDT chamber of small wheels. The maximum drift time of the tube is about 700 ns. The signals from muon tracks are masked by hits from preceeding cavern background hits. This is the main cause of the linear drop of tube efficiency as the tube rate increases. Decrease of tube efficiency and increase of tube occupancy both due to background hits together lead to a loss of segment reconstruction efficinecy. With the tube rate above $\sim$300kHz, the segment inefficiency becomes sizable and results in a degradation of spectrometer performance.

High background rate also causes degradation of position resolution arising from fluctuation of slow drifting positive ions affecting the drift electric field.

The CSC chambers are used in the small radius region of small wheel.

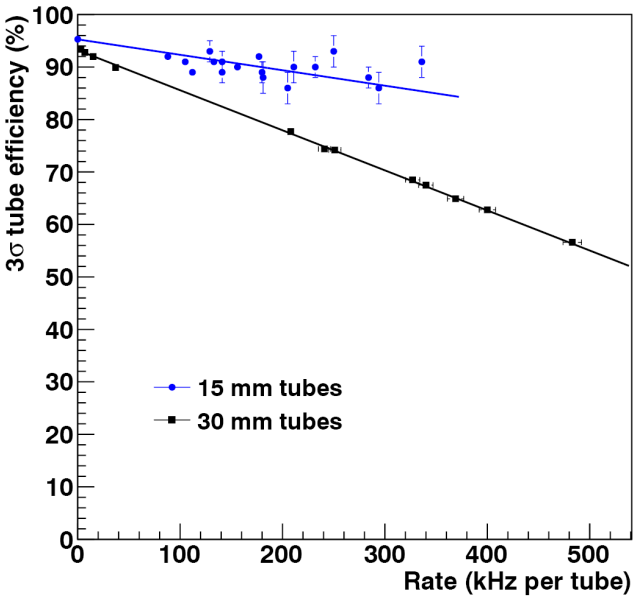

Figure 3: MDT tube efficiency vs hit rate for 30mm and 15mm tubes.

2.2 Level-1 muon trigger

ATLAS trigger is organized in 3-levels: level-1 (L1), level-2 (L2) and event filter (EF). The L1 trigger is the first step and it is based on information from muon spectrometer and calorimeter. The rate of L1 trigger is limited at 75kHz, and rate of EF output for permanent storage at ∼300 Hz

Triggering on leptons of $p_T \sim 20$ GeV is importnat for many searches as well as measurements of the SM processes. In the current running condition of the LHC at $\sqrt{s} = 7$ TeV and luminosity $1 \times 10^{33}\text{cm}^{-2}\text{s}^{-1}$, rate of L1 single muon trigger with p_T threshold of 20 GeV (L1MU20) is ~ 1 kHz. This rate can be compared to the rate of corresponding EF output for inclusive single muons with p_T threshold at 20 GeV, which is $\sim$ 25Hz. EF uses reconstruction using full detector information and the p_T is close to the offline reconstruction with good muon purity of over 90%. Using these observed numbers, we can make a rough estimation of trigger rate at higher luminosity as summarised in table 2.2. The rate of L1MU20 would saturate the total L1 rate at L=3×10^{34} and therefore this trigger cannot be used as it is now. The EF rate which is close to the true muon rate is still sufficiently low for a L1 trigger. There is a room for improvement of L1 trigger so that the rate would be acceptable even at the highesst luminosity after the phase-2 upgrade.

	1×10^{33}	1×10^{34}	3×10^{34}	5×10^{34}
L1 (kHz)	1	20	60	100
EF (Hz)	25	1,000	1,500	2,500

Table 1: caption

The L1 muon rate is dominated by the contribution from the endcap region. Figure 4

shows the η distribution of RoI for L1MU20 [1]. About 90% of the L1MU20 is from the endcaps ($|\eta| > 1.05$).

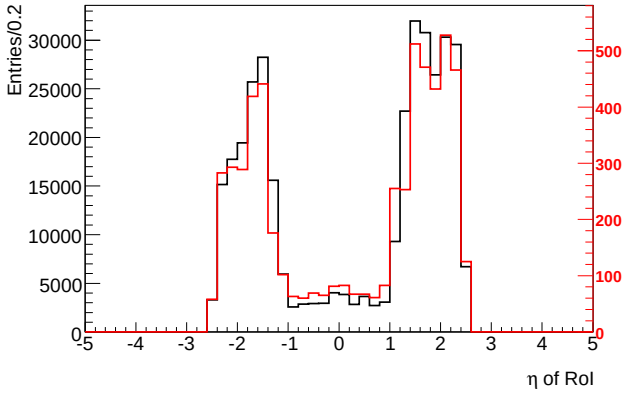

Figure 4: Distribution of L1 muon signal ($P_T > 20$ GeV) as a function of $|\eta|$. The black histogram is 2010 data while the red histogram is 2011 data.

Offline data analysis using the collision data have shown a number of interesting observations. There are large contribution from fake triggers in the endcap region. About 40% of L1MU20 has no corresponding EI segments (MDT or CSC) as shown in figure 5. Figure 5 shows how the rate reduces by successive application of requirements on the EI segments. By requiring EI segments which are pointing to IP and matched to the EM segments which produced the L1 trigger, the rate of the L1MU20 reduces to about 15%. Figure 5 also shows the

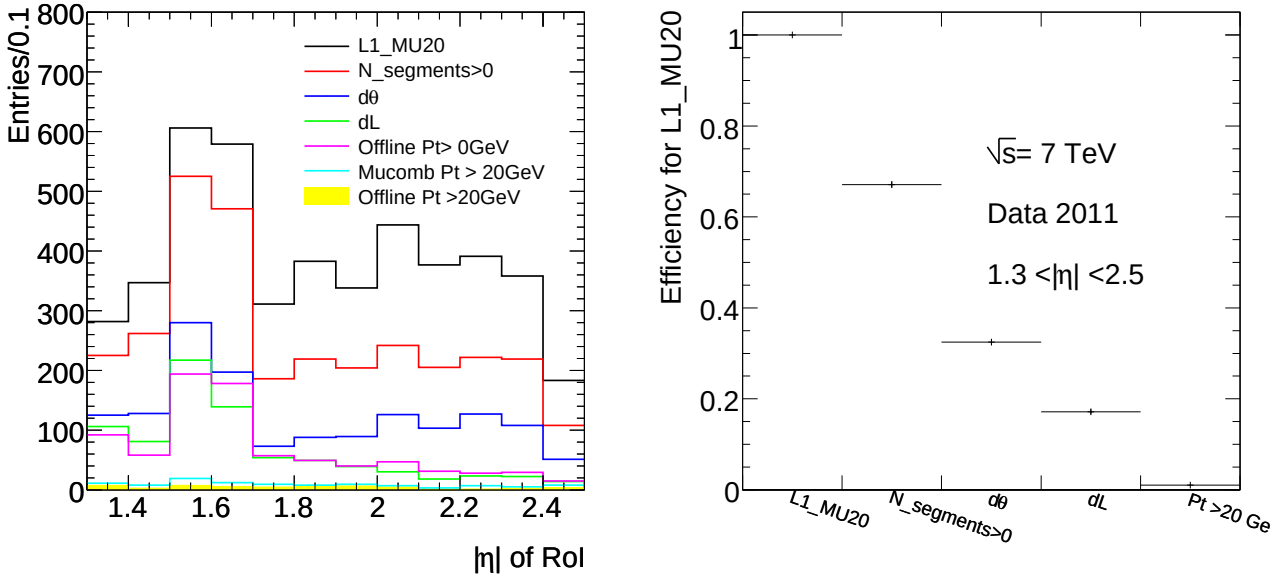

Figure 5: To test how to put figures.

fraction of off-line combined tracks and combined tracks having their p_T greater than 20 GeV,

[1] Currently L1MU20 is not used for L1 trigger. The figure shows the η distribution of L1MU20 signal in the data sample triggered by L1MU10 (P_T threshold at 10 GeV) with prescaling.

as it should from the definition of the trigger threshold. Possibility of further reducing the rate close to the rate of combined track will be discussed later in this section.

The sources of the abundant contribution from background has also been studied using the collision data. The nature of tracks of the EM segments without corresponding EI segments have been investigated using its timing and pulse-height information recorded by the MDT chambers. From time-of-flight of such particles detected by both EM and EO chambers correspond to particles with lower velocity, typically $\beta \sim 0.7$. Timing at EO station with respect to the beam crossing timing also suggest that these particles are slow particles. Currently a hypothesis is that these particles are low momentum protons created somewhere between the EI and EM statisons, either in the radiation shielding around the beam pipe or inside the materials of endcap toroidal coil, and had by chance created segments in EM which are approximately pointing toward the IP thus faking high p_T muons from the IP. This is shown schematically in Figure 6. The track 'B' is an example of slow protons produced in the region between EI and EM. There can also be a possibility of track 'C'. Such track may originate from beam halo. However, an investigation of events from non-colliding bunches has shown that such contribution is very small.

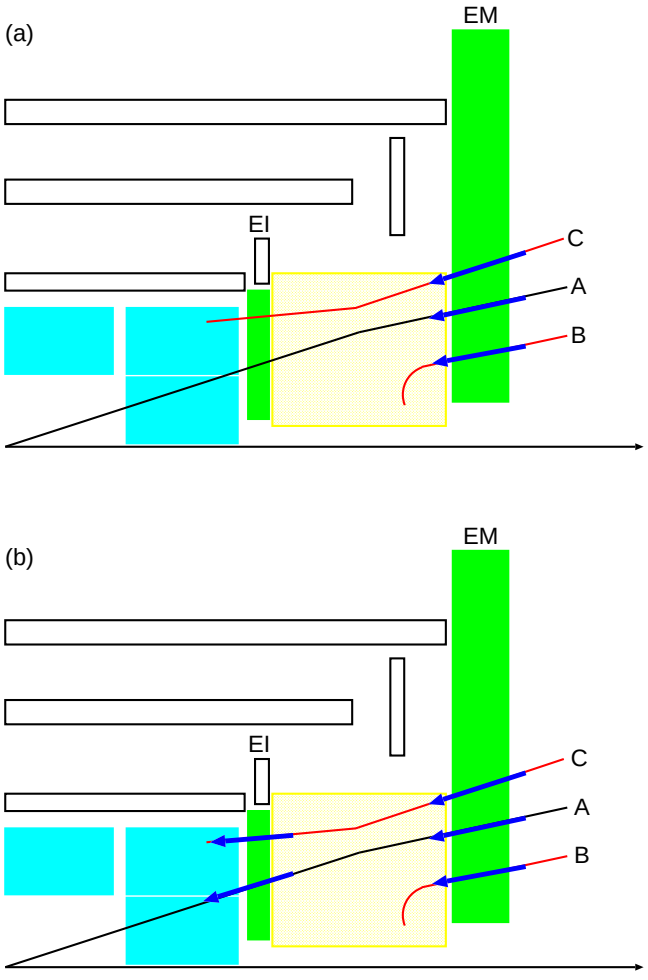

Figure 6: L1 trigger upgrade to purify high PT muon trigger.

Discussion of muon spectrometer performance at high luminosity - precision tracking and L1 trigger, and conclude that new detector and electronics are needed.

Point out serious (?) performance degradation in the small wheel region in both MDT and CSC, referring to the radiation background discussoin in Appendix. Performance of the present detector should be evaluated for high lumi conditin, either using high lumi Monte Carlo or overlay of real events. CSC is 4 layers.

In the L1 discussion, emphasise the importance of maintaining low p_T threshold. There are two issues.the high rate of fake triggers in the endcap region based mainly on the study using data. Then introduce basic idea of how this can be mitigated by integrating the small wheel in the L1 trigger. As the second point of trigger, discuss the pT resolution and possible improvement using the new small wheel. Physics requirement asks low pT threshold (20-40 GeV), L1 rate should be maintained at 100 kHz. Need sharpening pT threshold. Here introduce 1 mrad requirement.

Finally conclude that NSW should be built and replace the present ones as a phase-1 upgrade item in preparation to running with luminosity beyond the nominal luminosity.

3 Requirements for the new small wheel [LP]

In this section the requirements that the New Small Wheel have to meet are discussed. They are divided in three main categories: requirements on the rate capabilities and on the aging characteristics of the proposed detectors, requirements on the performance of the new system and requirement on the triggering capabilities of the new small wheel. During the period between the first LHC long shut down (2013-14) and the second long shut down foreseen in 2017 the machine luminosity will reach it's nominal value $1 \times 10^{34}\text{cm}^{-2}\text{s}^{-1}$, and then further ramp up to 2-3$\times 10^{34}\text{cm}^{-2}\text{s}^{-1}$, allowing the experiments to collect an integrated luminosity of a few 100 fb^{-1} within a few years. The phase-2 upgrade will then follow increasing the machine luminosity up to $5 \times 10^{34}\text{cm}^{-2}\text{s}^{-1}$ with luminosity leveling aiming at collecting 3000 fb^{-1} in $\sim$10 years. The New Small Wheel project is aimed at a detector that is able to collect high quality data also after phase-2, so the requirements are intended for a luminosity of $5 \times 10^{34}\text{cm}^{-2}\text{s}^{-1}$ and an integrated luminosity collected over more than 10 years of 3000 fb^{-1}.

3.1 Radiation environment

The New Small Wheel should be able to efficiently track muos up to luminosities of 5×10^{34} $\text{cm}^{-2}\text{s}^{-1}$. The hit rates at this luminosity can be inferred by extrapolating the present measurements, obtained at an average luminosity of 5.5×10^{32} $\text{cm}^{-2}\text{s}^{-1}$, taking advantage from the proportionality between hit rates and luminosity measured over 3-4 orders of magnitude as shown in **??**, and from the measurements of the hit rates versus the radial distance from the beam line **??**. The total hit rates extrapolated from the current measurements are shown in different regions of the detector in the table below:

Region	Rate(Hz/cm^{-2})
CSC	7000
EIL1	3600
EIL2	1100

It should be noted that the current extrapolation does not take into account the fact that in 2013-14 the beam pipe will be replaced with a lighter one, which entails, following simulations, a decrease in the total cavern background of about 1.2-1.3 and the increase of beam energy of a factor 2. Simulations indicate that the increase in cavern background due to the increase in beam energy are expected to be roughly a factor 1.6.

The uncertainties in these two effects and in the extrapolation from 5.5×10^{33} $\text{cm}^{-2}\text{s}^{-1}$ to 5×10^{34} $\text{cm}^{-2}\text{s}^{-1}$, can be summarized in a safety factor of 2, so the New Smalll Wheel should be designed to cope with the rates indicated in the following Table:

Region	Rate(Hz/cm^{-2})
CSC	14000
EIL1	7200
EIL2	2200

It should be noted that at the smaller radius foreseen for the detectors (80 cm from the beam pipe) the extrapolated rate is close to 20 kHz cm^{-2}.

3.2 Detector ageing

The New Small Wheel should be able to take good quality data over the full period of LHC exploitation (including Phase 2) This means that the integrated luminosity will be about 3000 fb^{-1}. Using the previous tables on hit rates and assuming ten years of operation with 10^7 seconds per year the total number of hits per unit area in the hottest region will be about 10^{12}. For a detector that produces on average100 electrons of ionization with an amplification factor of 10^4, a total collected charge of about 0.2 Coulomb/cm^2 in the CSC region is expected. The proposed detectors should be validated for ageing effects at a level of about 1 Coulomb/cm^{-2} or higher, and in case the required lifetime would be difficult to achieve, the possibility of replacing chambers, especially in the very forward region, should be envisaged. The trigger and read-out electronics should be validated as well for particle fluences compatible with the above figures. There should also be the possibility to place the read-out electronics in places where the particle flux is smaller (e.g at larger radius compared to the position of the chambers)

3.3 Radiation shielding

The mechanical structure should contain radiation shielding to protect the small wheel detector and other part of the muon system. Shielding layout is an integral part of the small wheel structure, design of detector mechanics, its support structure and shielding have to be considered together.

1. Performance of radiation shielding should be at least as good as the present installation.
2. Possibility of improved shielding should be studied, which would be installed in the small wheel structure and protect the muon detector in general as well as the small wheel detector and electronics.

The present idea is to retain the structure of the JD shielding. Possibility of additional shielding materials, e.g. polyethylene cladding on the surface of JD disk, should be studied to further improve radiation shielding. Another possibility is a small photon shielding around the beam pipe in the region of small (7 cm) gap between endcap calorimeter and JD disk. This may help reducing photons channelling through the calorimeter-JD gap and hitting the barrel chambers at $|z| \approx 7$m.

3.4 Detector performance

3.4.1 Detector coverage

1. The large-small layout should be maintained in the new small wheel unless there is a strong reason for other layout

2. Active area of the detector for precision tracking should cover full azimuthal and the same η range as that of the present small wheel without any geometrical gap for high p_T particles from IP.

3. The same requirement applies also to the coverage of L1 trigger, but its η coverage may be adjusted to match the acceptance of endcap L1 trigger.

3.4.2 Tracking performance

Here summarized are the requirements on segment reconstruction for precision muon tracking.

1. Performance in the bending plane

   The new detector should have its performance at high luminosity at least as good as the present detector operated at low luminosity.

   - Segment position resolution - 60 μm.
   - Segment angular resolution - 0.3 milliradian.
   - Segment finding efficiency and resolution at least as good as the present MDT chamber at low luminosity- ¿ 97% and superpoint resolution $\simeq$ 50 μm.

   The efficiency figure is required for muons with $p_T > 10$ GeV. The resolution figure is required for $p_T >$50 GeV. Size of multiple scattering in the endcap toroid is 0.4 milliradian for p=150 GeV and 2 milliradian for p =30 GeV, each roughly at the centre of the toroid. This sets a scale of required angular resolution for segments. Efficiency should not degrade at very high momenta (δ-ray, showers,.)

2. Performance in the second coordinate

   Relaxed requirements - position resolution of a few mm.

3. Pads

   Additional studies are needed to assess the usefulness of pads that would reduce the amount of ghosts in 2-d. At present we estimate that pads of some 100 cm^2 would be beneficial.

4. Fake segments

   Sensitivity to fake segments, related to combinatorial and cavern background, should be optimized in order to maintain their frequency comparable to real tracks and not to affect the track reconstruction performance.

Detailed studies should be made further in order to better understand the required and expected performance. The following are a few potentially important parameters determining the performance:

- number of layers
- two track separation
- pads or other means of ghost removal.

3.5 Level-1 trigger function

The small wheel detector and associated electronics should provide information for the L1 trigger upgrade in the endcap. The position and angle of small wheel segments are used to improve the quality of L1 high p_T decision by the big wheel TGCs.

1. The system should perform real-time reconstruction of track segments which are approximately pointing to the IP. The acceptance angle should be optimised taking into account the expected angular range of good tracks from IP, detector alignment error, complexity of implementation and any physics requirements.
2. For each segment, a set of data (R, ϕ, $\Delta\theta$), or an equivalent set of information, should be provided. Here radial and azimuthal coordinates R and ϕ represent the position of the segment on small wheel at appropriately defined z coordinate Z. The quantity $\Delta\theta$ is a measure of how well the reconstructed segment is pointing to the nominal IP - the difference of segment polar angle with respect to the angle $\tan^{-1}(R/Z)$.
3. The track segment data (R, ϕ, $\Delta\theta$) should be transmitted to the trigger logic of corresponding trigger sector(s), where final endcap L1 signal is constructed (sector logic). Details such as maximum number of segments, data format and data transfer protocol are to be defined in the framework of overall trigger electronics design.
4. Angular resolution of $\Delta\theta$ must be 1 milliradian (RMS) or better.
5. Granularity of R and ϕ information should be matched to the size of ROI of the present endcap trigger (0.04×0.04 in η-ϕ).
6. The (R, ϕ, $\Delta\theta$) information should arrive the input of sector logic not later than the arrival time of the main trigger inputs from the big wheel TGC. The delay of the TGC signal is at present 1.088 μsec from the collision.
7. Efficiency of segment reconstruction should be high and robust. Rate of fake segments should be optimised so as not to affect significantly the trigger efficiency while maintaining good rejection power of fake L1 triggers.

This implies that the number of detector layers should not be too small - many layers will bring high efficiency, low fake rate, good angular resolution and also operational robustness due to redundancy. Long lever arm will be beneficial especially for angular resolution. Optimisation should be made taking into account elements including performance, complexity and limitations from available space which is shared by the detector and possible installation of additional shielding.

3.6 Alignment

1. As in the present small wheel, an optical alignment device should be installed and integrated as a part of the endcap optical alignment system. This requirement imposes geometrical constraint on the mechanical structure and on the placement of the New Small Wheel chambers since the full compatibility with the present alignment system requires to place the alignment bars in well defined positions.

2. In addition, there must be a mechanism to provide internal alignment within each chamber module. This is particularly important for detectors where deformation is foreseen due to effects such as gravity, temperature change and magnetic field.

Chamber design should proceed in close collaboration with the alignment group in such a way that all the details of the relative alignment of different detector layers are taken into account at design stage.

4 General Detector ..... [JD]

There are n proposed detector concepts which are discussed in next sections. Here, the following 3 points can be discussed commonly.

4.1 Mechanical structure

8+8 large-small layout, total space in z and R. Support structure, accessibility, ..

4.2 Radiation shielding

The same as now, or possible improvement of radiation shielding, ..

4.3 Alignment

Requirements, target figures, important comments which can be made independent of the detail of detector layout.

4.4 Readout electronics

Issues common to all concept. Around ROD.

4.5 DCS, services,

5 Detector concept 1 : MDT + TGC (working title)

This section will be merged with the next section into a single section and appendix.

Introduction to this concept: This section should describe the technology concept, details up to the level of a single chamber should be given in the appropriate appendix.

5.1 Introduction

The Small Wheel (SW) is the first station ("Inner station") in the end-cap of the Muon spectrometer. Together with the Middle and Outer station it delivers the spatial coordinates for the momentum determination of charged tracks. Between the Small Wheel and the Middle station ("Big Wheel") a toroidal magnet is located with a bending power ranging from 3–7 T $\times$ m, depending on η, allowing a determination of the track momentum with high accuracy.

Designed to measure the momentum of a charged particle, the three stations of the end-cap have two distinct functions. They provide a fast, raw determination of the transverse momentum p_T, shortly after the passage of the particle, to be used by the Level-1 (L1) trigger. The L1 trigger logic has the task to identify events of physics interest, for which a high-p_T muon is a crucial signature.

When a L1 trigger decision is broadcast to the ATLAS subsystems, the DAQ has to retain all relevant information for the corresponding beam crossing (BX). Because of technical limitations on data storage of the electronics, however, the L1-trigger must arrive at the subdetectors not later than 2,5 μs after particle passage, otherwise the information might be lost (trigger "latency"). This short L1 trigger latency of the present ATLAS readout system strongly limits the selectivity of the L1 decision, as only a fraction of the available tracking information can be used for a reduction of fake triggers, which are mainly due to low-p_T tracks. One of the design aims for the ATLAS upgrade in phase II is an increase of the L1 trigger latency to 6,4 μs or even up to 10 μs. At this point more selective trigger strategies can be implemented, partly at the level of the frontend electronics, partly at the level of the Central Trigger Processor (CTP), where trigger information from different subdetectors can be combined.

The second important function of the three stations in the muon end-cap is the measurement of the momentum with the highest available spatial accuracy. This is achieved by combining high resolution drift tube chambers with a precise optical alignment system. The relative positions of track hits in front and behind the bending magnet are thus precisely known, resulting in the required momentum resolution.

In the present Small Wheel Thin Gap Chambers (TGC) are used for the selection of high-p_T tracks for the L1-trigger, while Monitored Drift Tube chambers (MDT) are used for the precision determination of the track coordinates.

The LHC upgrade in phase I and II will lead to an increase of the instantaneous luminosity by a factor of 2 (respectively 5). In the present SW, these high luminosities and the resulting background rates of will lead to an unacceptable reduction in trigger and tracking efficiency. In the following we present a overview of the main shortcomings of the existing SW.

5.1.1 Problems of Small Wheel chambers at high background

The present L1-trigger in the end-cap suffers from the fact that a majority of tracks crossing the SW do not come from the primary vertex and should therefore not be used as parts of a high-p_T muon candidates by the triggering system. The present trigger does not allow not to determine the slope of the candidate track and can not discard tracks which do not come from the primary vertex. Newly designed trigger chambers will have to be able to determine the slope of the track with an accuracy of < 1 mrad in the r-z plane (bending plane). The slope must also be determined in the ϕ direction, though with less accuracy, to further reduce the number of trigger candidates which do not come from the interaction point.

The MDT precision chambers will start to lose efficiency if hit rates go beyond about 300 kHz per tube. The large majority of hits in the MDT are coming from gamma and neutron conversions in support structures, tube walls, chamber gas and tungsten wires. With a diameter of 30 mm and a length of 60–250 cm (??), MDT chambers see hit rates of up to 300 kHz per tube, which comes close to what the readout system can handle without losses. While the length of the tubes in the trapezoidal geometry of the SW decreases proportional to r, the BG rates increase considerably faster than with 1/r. Thus the highest hit rates per tube occur at the inner tip of of the EIS and EIL chambers.

Chamber Type	location in r	tube length	expected hit rate	rate per tube	occup-ancy	effi-ciency
	cm	*cm*	*hits/cm²*	*kHz*	*%*	*%*
EIL0	150 cm	75 cm ??	2000	2 kHz	85 %	xx
EIL1	262 cm	152 cm	300	0,3 kHz	92 %	xx
EIL2	373 cm	206 cm	100	0,1 kHz	98 %	xx

Table 2: Expected hit rates and efficiencies for 15 mm tubes in the NSW. (Numbers are mostly dummies and have to be worked out later!

High hit occupancies of the tubes lead to inefficiencies due to the reduction of the drift field and to space charge effects. In addition, the dead time induced into the electronics by a conversion hit may mask a subsequent "good" hit from a track.

Table 2 gives background rates, occupancies and hit efficiencies for MDT tubes at different radii in the SW, based on simulation work in Ref. [**?**]. Results form LHC running at luminosities up to 5×10^{32} seem to indicate rates which are about a factor 3–4 above the simulated ones for the innermost chambers EIS1 and EIL1 of the SW.

5.1.2 Concept for a New Small Wheel

Tu cure the shortcomings of the existing system, a new concept is proposed for the Inner station, the New Small Wheel (NSW). For the trigger chambers we propose to maintain the basic operating concept of TGC chambers, complementing them with a new, high-performance readout system. The pulseheight distribution of signals induced into the strips of the TGC cathodes (measuring η) are convoluted to give the precision coordinate with an accuracy of $<$100 μm. With modern, radiation-tolerant FPGAs the location of the hits can be determined

fast enough for the L1 trigger. In the proposed detector layout, a package of 4 TGC chambers is placed in front and behind the MDT chambers, each. A TGC package will contain 4 wire layers (wires running radially, perpendicular to the strips), 4 cathode layers for centroide finding and another 4 cathode layers segmented into pads for fast selection of a Region of Interest (RoI). In the offline analysis the pads will be an important tool for resolving ambiguities in the x-y pairing of coordinates, when more than one track is present in a chamber. With a distance of about 300 mm between the TGC packages in front and behind the MDT, an angular resolution of $< 0,3$ mrad can be achieved. Only tracks pointing to the interaction point will be considered as high-p_T candidates for the L1 trigger. A detailed presentation of the method is given in section 5.4.

The problem of high tube occupancies of the MDT is solved by using a newly developed type of MDT drift tubes, the tube diameter being reduced from 30 mm to 15 mm. While the tube area exposed to background radiation is thus reduced by a factor of two, the maximum drift time is reduced by a factor of 3,5 (750 ns to 200 ns), the combined effect giving a reduction of hit rates by a factor of 7. The mechanical structure and the alignment system will be as similar as possible to the ones in the present SW architecture. Like in the case of the TGCs, faster readout electronics has to be installed, see section 5.5.

Both new chamber systems, the TGCs and the MDTs, can be operated with the same chamber gas as in the present system. Power requirements for the electronics of both systems will be higher due to higher channel count. Whether this requires active cooling, as is now used in the region $\eta > 2$ ("CSC region") is under study. Aim is to have services arranged in such a way as to be able to use the existing service infrastructure like e.g. the cable Schlepps.

5.2 Detector technology and layout

Description of detector concept (a detailed description of the working principle of each detector should be given as an appendix).
If more than 1 technology is used motivate the decision and detail how they work together (e.g. can services be shared, is the information of the trigger chambers used in the precision chambers, how are combined chambers assembled etc.)

List of all operating parameters
Detailed layout: acceptance, description of chamber overlap and dead areas, drawings
Tables with chambers sizes, number of channels
Internal alignment scheme (the overall common endcap alignment scheme is described in the previous chapter)
Calculations about mechanical stability and expected deformations due to gravity, temperature changes, (magnetic field) etc.
Requirements for mount points
Details of service points and other positions where access is needed
Concept for chamber replacement (what needs to be dismounted etc.)

5.2.1 Upgrade of the LHC towards higher Luminosities

For use at the future Super-LHC a new type of muon detector has been developed. It is based on the proven MDT drift tube design, but with tubes of half the diameter, leading to higher rate capabilities by an order of magnitude. We present test results on efficiency and position resolution at high background rates and describe the practical implementation in a real-size prototype.

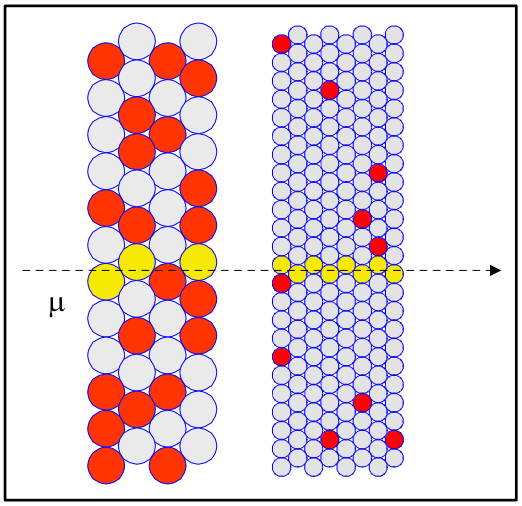

Figure 7: The tracking quality in 30 mm and 15 mm drift tubes in a region of high n/γ background. The occupancies from background hits (red dots) are 50% in the 30 mm tubes but only 7% in the 15 mm tubes due to shorter drift time and smaller area.

At luminosities far beyond the original design value of 10^{34} cm^{-2}s^{-1} the MDT drift tube chambers will face the challenge to maintain excellent tracking efficiency in the presence of high background hit rates, due to gamma conversions.

5.2.2 Tracking in a high–background environment

The outer region of the ATLAS detector, where the muon chambers are located, receives high rates of low-energy neutrons, mainly due to shower leakage from calorimeters and shielding structures in the high-η region. At the nominal luminosity, gammas from neutron capture and related conversion electrons are expected to generate hit rates in the range 50–300 kHz in each MDT tube. A conversion electron may create an inefficiency if the signal arrives *before* the muon signal. The muon detection efficiency thus becomes exp(-τ×f) ≈ 1-τ×f, where τ is the average drift time in the MDT tubes and f the hit rate due to gamma conversions.

At high rates of n/γ background, the efficiency may be further reduced by a decrease of the gas amplification due to space charge from slowly drifting positive ions in the tubes, while the *fluctuations* of the space charge tend to degrade the spatial resolution by up to about 20 % at the highest rates.

The effects of gamma conversions in the MDT tubes have been studied in detail using a muon beam in the presence of intense γ-irradiation of up to 500 Hz/cm^2 (i.e. ∼300 kHz/tube),

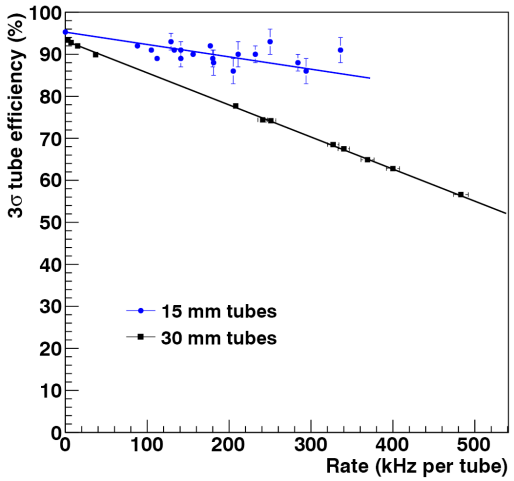

Figure 8: Efficiency vs. hit rate per tube for 30 mm and 15 mm drift tubes.

as delivered by the Gamma Irradiation Facility at CERN (GIF) [**?**]. While the γ-rates at the GIF correspond to only about 30 % of the background levels expected for the hottest regions at the SLHC, the results of these measurements already allow to define the baseline of a chamber design with much improved tracking capability: MDT drift tubes with only half the tube diameter offer a reduction of the drift time by a factor 3.5, due to the non-linear relation between track distance from the central wire and drift time (r-t relation) and in addition by a factor 2 from the exposed area, thus yielding a factor 7 in the reduction of the hit rate due to n/γ background. Moreover, up to two times more tube layers can in principle be accommodated in the available space, leading to improved track finding efficiency and position resolution (see Fig. 1).

The reduction of the tube diameter of the MDT tubes allows to maintain the main advantages of the drift tube concept: (a) independence of the position resolution from the angle of incidence onto the chamber plane (contrary to drift chambers with rectangular drift geometry) (b) operational independance of each tube, where any malfunction of a tube can only generate a negligible inefficiency (c) modularity of chamber construction.

To verify the performance of 15 mm ("small") tubes a number of tests was executed, using cosmic muon tracks. A pair of 30 mm ("large") drift tube chambers was used as reference, defining the position of the muon track, while a layer of small tubes was the device under test. Tubes along the track are called 'efficient' when the hit is detected inside a 3σ road, as defined by the reference tubes.

This measurement was done in the presence of adjustable levels of gamma background due to the GIF facility at CERN [**?**]. Fig. 8 shows the efficiency of small and large tubes vs. hit rate from gamma conversions. As expected, small tubes provide a much better performance at high background rates. The efficiency at rate zero deviates from 100 % due to tracks passing across or close to the tube walls and due to δ-electrons shifting the hit position outside the 3σ acceptance road. The average position resolution in the small tubes was about 120 μm. Due to the short drift compared to large tubes, this value showed little dependence on the background rate.

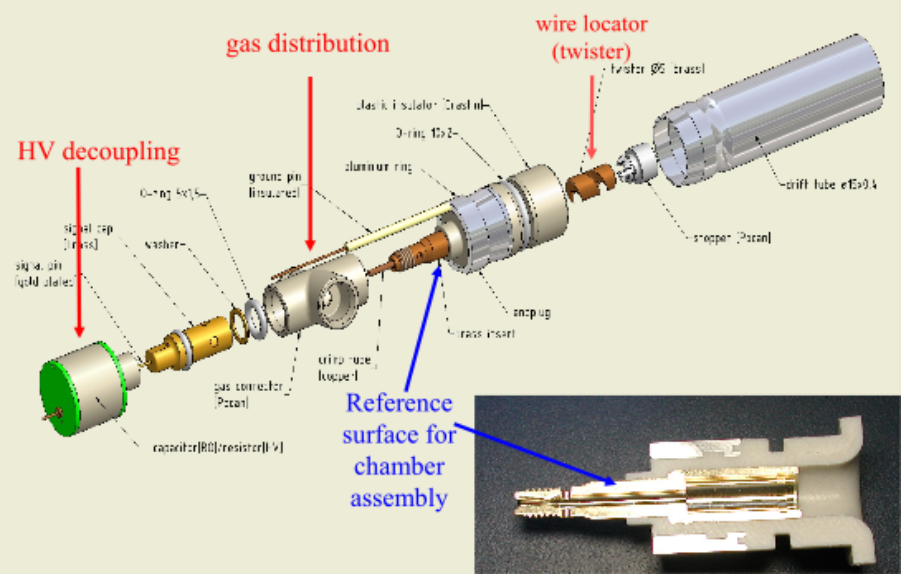

Figure 9: Structure of a small drift tube with gas connection and decoupling capacitor in the longitudinal direction (green cylinder). The plastic parts are injection moulded.

5.2.3 Technical Implementation

Going from large to small tubes as construction elements for MDT chambers poses a number of technical challenges, as the higher tube density requires more refined electrical and gas connections on the same available service area.

A particular problem is the supply of the tubes with the operating voltage of 2730 V, requiring isolation distances which cannot be realized on the area available for the readout boards. The integration of the HV decoupling capacitors into the end-plugs of the tubes was therefore a central requirement for the tubes. In a similar way, gas supplies had to be simplified to facilitate the integration of the tubes. Fig. 3 shows the tube design, HV capacitor and gas distribution being integrated into the structure of the end-plug.

The integration of tubes into chambers is achieved by bonding tubes layer by layer with epoxy glue. In production tests, tubes were fixed in precision supports ("combs") during curing, and the target accuracy of 20 μm was obtained. A module with 8 tube layers was glued in a time span of a few hours. With curing overnight, the assembly of a module took only one day.

Presently, a full prototype of a MDT chamber in small tube technology is under construction. It consists of 2×8 tube layers and is designed to fit into the inner part of the muon detector in the very forward direction, where rates are highest (Fig. 4). This prototype will be available for tests in a muon beam at CERN and in the GIF facility in summer 2010. The readout will be achieved with available electronics for the large tube chambers, specially adapted for use with the new chamber geometry.

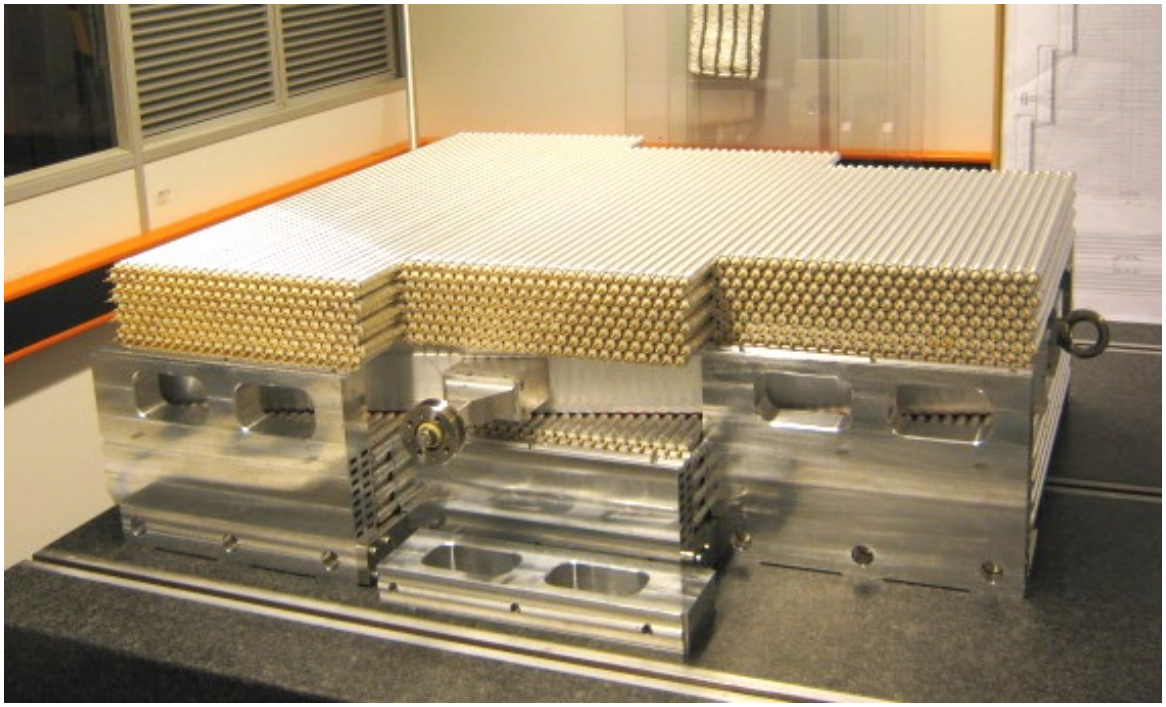

Figure 10: The small tube prototype chamber after assembly, consisting of two modules of 8 tube layers, 72 tubes per layer and 1152 tubes in total.

5.3 Performance

Summary of chamber performance, details in appendix of technology.

1. *Spatial and angular resolution as functions of rate and angle of incidence*
2. *Time resolution*
3. *Efficiency (single measurement and segment)*
4. *Double track resolution*
5. *Rejection of fake and background tracks*

5.4 L1 trigger and electronics

1. *How the L1 signal are produced, starting from the detector signal till the formation of SL input.*
2. *Latency (calculation, measurement with demonstrator)*
3. *Compatibility with Phase II upgrade !!! RR to supply text !!!*

5.5 Readout electronics and integration in DAQ

Detailed description of electronics chain.– Integration to DAQ (Mention the GBT?).– Readout related parameters, e.g. bandwidth requirements, number and granularity of read-out links.– Compatibility with Phase II upgrade.

The readout of the Small MDT tubes follows the proven architecture of the present MDT system, however, a number of modifications and additions is required to improve the rate capability and to adapt the layout to the four times higher channel density on the front faces of the Small tube chambers.

In the present readout scheme tube signals are routed via a PCB ("hedgehog card") to a piggy-back card ("mezzanine card"), containing an Amplifier and Shaper, followed by a Discriminator with adjustable threshold, all three functions being integrated in a radiation tolerant ASIC (ASD). The discriminator outputs, in turn, are routed to a TDC, where each leading and trailing edge signal receives a high-precision time stamp, which is retained, together with the corresponding channel number, in a large internal buffer of the TDC ("Level-1 buffer").

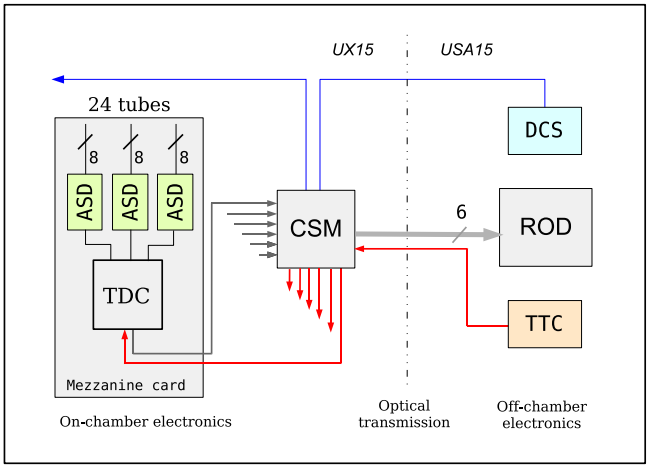

Figure 11: Schematic diagram of the present MDT readout chain. The Chamber Service Module (CSM) collects all data of a given chamber and sends them to the ROD via an optical link. Up to 18 TDCs, corresponding to 432 tubes, can be serviced by a CSM. The 40 MHz clock and the Level-1 trigger are broadcast by the TTC system to the TDCs.

When the TDC receives a Level-1 trigger, a subset of the recorded hits, corresponding to a pre-defined time window, are retained for readout. These data are forwarded to the data concentrator of this chamber, the "Chamber Service Module" (CSM). From there, data are sent to the off-chamber electronics in USA15, the "Readout Driver" (ROD). A CSM can serve up to 18 mezzanine cards. The operation parameters of the analog frontend (ASD) and the TDC are controlled by a JTAG string, which is distributed by DCS via CSM, individually to each mezzanine card. Fig. 11 gives the layout of the present system. A detailed presentation of the MDT readout electronics is given in [**?**]. The ASD and TDC ASICs are described in [**?**] and [**?**].

For an evolution of this architecture into matching the requirements of the Small tube readout, a number of problems limiting the performance of the present scheme has to be

overcome. Given the high rate capability of the Small MDT tubes, a higher bandwidth of the readout system has to be achieved. Due to the limitations of the internal buffering scheme and processing speed, the present TDC can only handle average tube rates up to about 300 kHz per tube without losing data, while Small tubes would operate beyond 1 MHz per tube. Therefore, an improved TDC is an essential requirement for a new readout design. Another limitation of the readout bandwidth comes from the optical link from CSM to ROD, the S-link protocol only supporting a usable bandwidth of 1,4 Gbit/s. Fig. 12 shows occupancy and efficiency of Large and Small tubes as a function of tube hit rate.

Apart from performance limitations, the presently used ASICs suffer from the fact that their technologies do no longer exist. In order to replace obsolete technologies, the following new components had therefore to be introduced into the new architecture.

- The ASD is re-designed in the IBM 130 nm technology. A 4-channel prototype, demonstrating the analog parameters, has already been produced and works correctly. Most analog parameters of the previous design are preserved.
- The TDC will be replaced by the HPTDC, designed by the CERN-MIC group ([**?**]). This is a 32-channel device with improved internal buffering and higher tranfer and processing rates.
- The link connecting the CSM to the ROD will be replaced by a GBT link, developed by CERN. This link provides a 3 times higher transfer rate (Gbit/s), compared to the S-link.

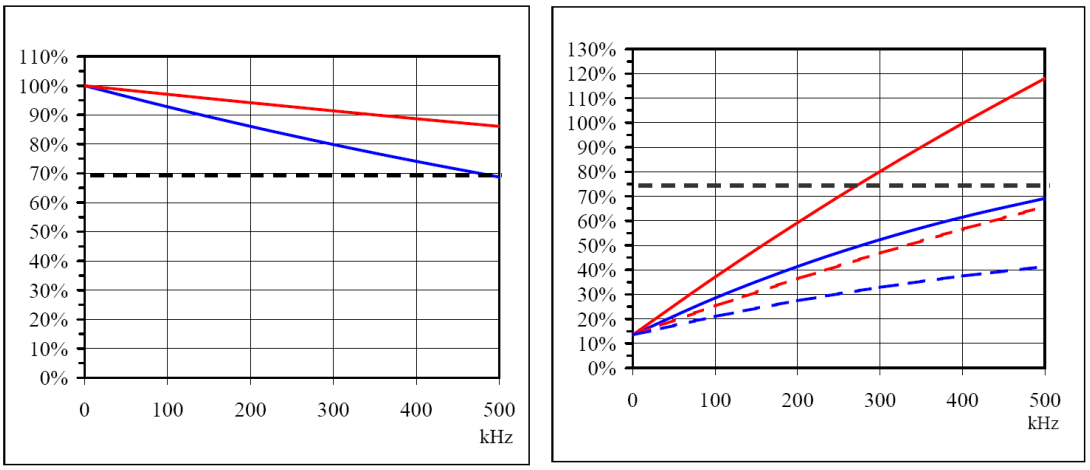

Figure 12: Efficiency (left) and saturation of the readout link between TDC and CSM in edge mode (right) as a function of the tube hit rate for dead time 750 ns (blue) and 200 ns (red). The dotted curves in the right diagram correspond to pair mode. The dotted horizontal line marks the minimum efficiency required for reliable tracking (left) and the maximum saturation level recommended for the readout. **This numbers will be checked. The diagrams will be simplified.**

Another stringent requirement for the practical realization of the new readout scheme is the mechanical integration of the on-chamber readout electronics with the chamber mechanics, as the density of channels on the chamber ends is four times higher than in the case of the Large tubes. The following design changes were therefore necessary.

- HV decoupling capacitors are located in 15 mm diameter cylinders at the tube ends, see Fig. 5.2.2. The density of signal routing on hedgehog cards is thus no longer limited by HV insulation distances between HV and signal traces on the PCB.
- The mezzanine card has to serve a four times higher channel density. We will change the ASDs into a 16-fold modularity and use the 32-channel HPTDC. To gain additional space, the passive protection circuitry of the ASD inputs will be moved to the hedgehog card.
- For the interconnection between mezzanine cards and New CSM we foresee to use the same 40-wire cables as was used in the present system. Its moderate diameter and high flexibility may be important for fitting the new MDTs into the limited space in the Small Wheel.
- While the power dissipation of the on-chamber frontend electronics of the present system was xx W/channel, leading to a dissipation of yy W/m in multilayers with 4 tube layers, the dissipation would now be about zz W/m. This may require flushing with dry air or even liquid cooling, as natural air convection is hampered by the tight space constraints of the Small Wheel.

Now something about mechanics, real estate, component density, packaging etc.

Finally something about rates.

5.6 Services, infrastructure, and DCS !!! RR+JD to supply text !!!

1. *Description of service scheme (including power system, read-out, trigger, alignment), cooling needs and other special requirements*
2. *Table with number of services (number of cables, outer diameter, cross section of leads)*
3. *Table with power consumption (per channel, chamber, total)*
4. *Required rack space*
   (a) *UX15 (include maximum allowed distance to detector if any)*
   (b) *US15 (power system)*
   (c) *USA15 (DAQ)*
5. *Gas system and distribution*
   Details on number of gas manifolds per sector (include drawings) and connections to chambers (serial, parallel?)). Size of pipes
   Required nominal, minimum, and maximum flow
   Required precision of gas mixture
   Safety measures in case of inflammable gas
   Required rack space for gas system in SGX1, USA15, UX15
6. *Integration in DCS system, requirements for DCS !!! Via GBT or ELMB++ ?? !!!*

Cable	Number of cables (granularity)	Outer cable diam. (mm)	Cross section of leads (mm^2))
HV			
LV			
Monitoring and control			
Front-end links			
Calibration			
Alignment			
Miscellaneous			

Table 3: Example table number of services per chamber

Chamber	Number of channels	Power consumption per channel	Total power consumption

Table 4: Example table: Number and types of chambers per sector

6 Detector concept 1 : MDT + TGC

This section will be merged with the previous section into a single section and appendix.

Introduction
The dominant motivation behind the present proposal is to keep the uniformity of the present MUON spectrometer (MDT as tracking detectors; RPC as trigger detectors in the barrel and TGCs in the End-Cap), while profiting from an extension of the present alignment system, as well as the existing technical infrastructure and experience to construct such an assembly at the relevant institutions.

The basic design consists of two packages of TGC detectors, each package containing 4 gas gaps of detectors, where each gap provides a pad, strip and wire readout (see Fig. 13).

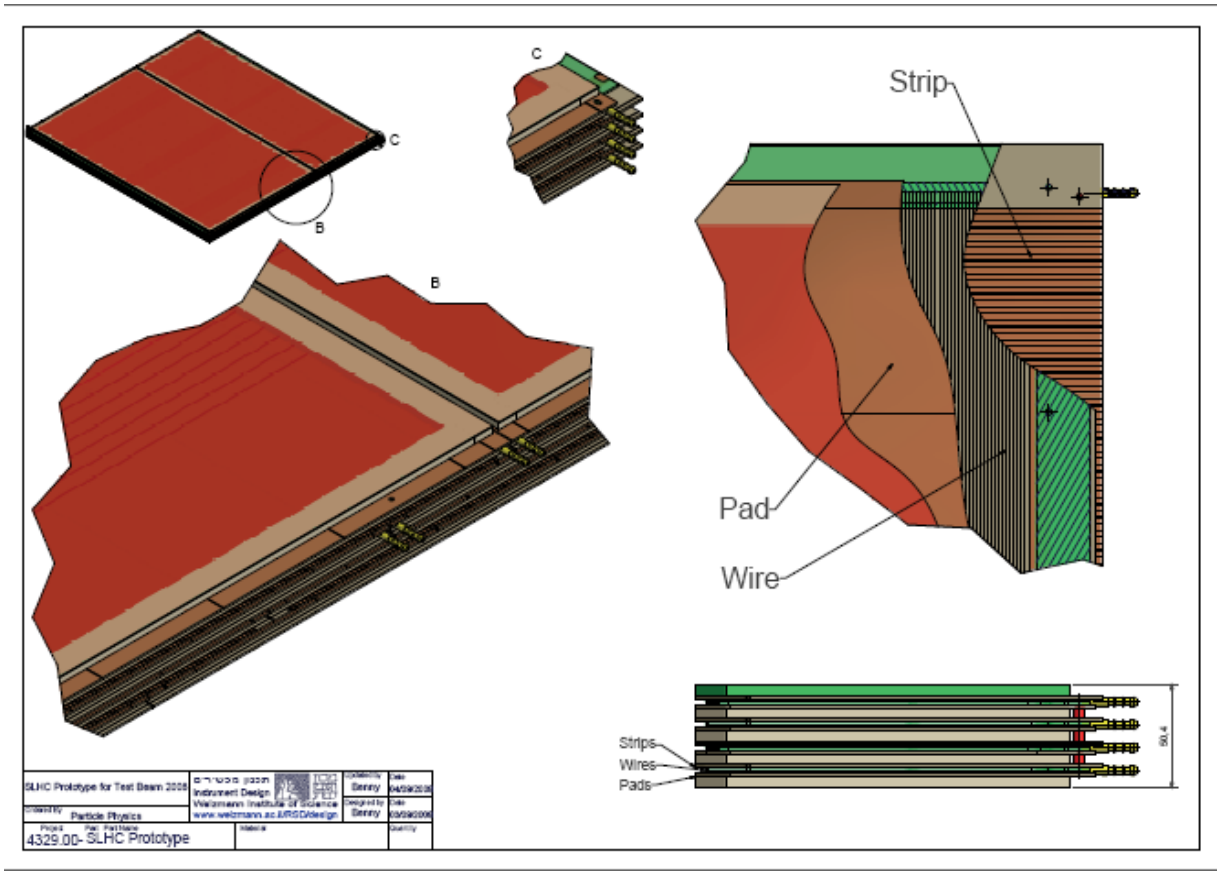

Figure 13: schematics of the internal layout of an individual package, showing the pad-strip and wire readout for each gas-gap.

By making a coincidence among the pads in successive layers (within a 1DEG aperture), one is able to reduce substantially the number of channels that have to be readout for a fast trigger decision; furthermore, the pad-coincidence provide a unique 3-D address, where a corresponding angle and displacement comparison can be made with the trigger input of the normal MUON End-Cap trigger originated in the ATLAS Big-Wheels. To simplify the logic of what channels to read for Trigger purposes, one might loose some of the potential MUON candidates, which can be recuperated by the measurements of the MDT (smaller number of channels). The MDTs

provide, furthermore an accurate alignment that can be used to align with tracks the exact TGC positions.

The basis of the proposed concept is to have as many as possible accurate measurements in the trigger layers, to allow to discard a high percentage of these measurements where δ-rays, additional γ's or neutrons are present and still obtain a position measurement from each of the two packages with a precision of 100μm. To obtain such a precision using the 3.5mm pitch strips present in each gas-gap, while keeping simple electronics, a charge extrapolation method using Time-Over-Threshold as an approximated charge measurement has been developed. The achieved performance using this method for large size TGCs is discussed in detail in 5.2. Achieving this high accuracy for the bending coordinate in each of the gas gaps allows the TGCs to provide a very good compliment to the MDT measurements (of similar precision) and reduce the number of tubes. In particular, in the high background rate region of the Small-Wheel, having a total of 16 potential measurement points, of which $\tilde{3}0\%$ will need to be discarded, ensure that an accurate particle vector will be provided in front of the End-Cap Toroidal field, even if some of the layers become non-operational during the exploitation of ATLAS at sLHC. The overall signal processing to produce the trigger is schematically shown in Fig. 14, based on a demonstrator that has recently been completed.

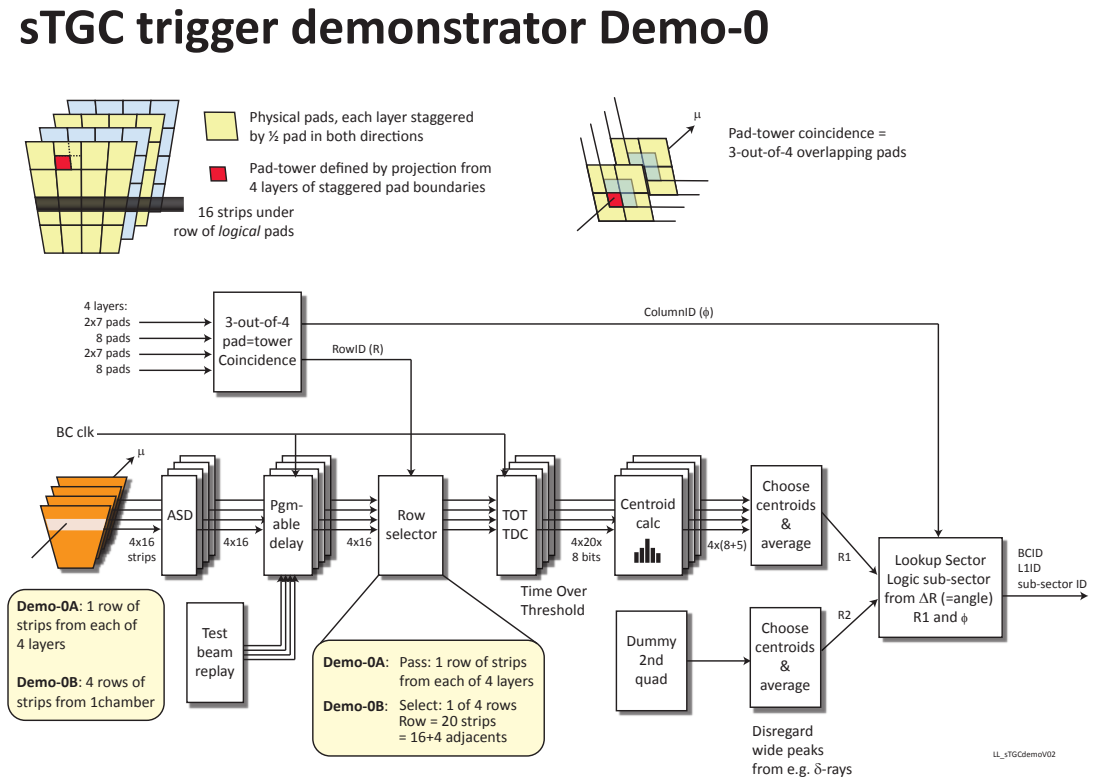

Figure 14: schematic layout of the trigger and readout as it is presently implemented in a demonstrator.

6.1 Detector technology and layout

Fig. 15 shows a schematic layout of the proposed detection system.

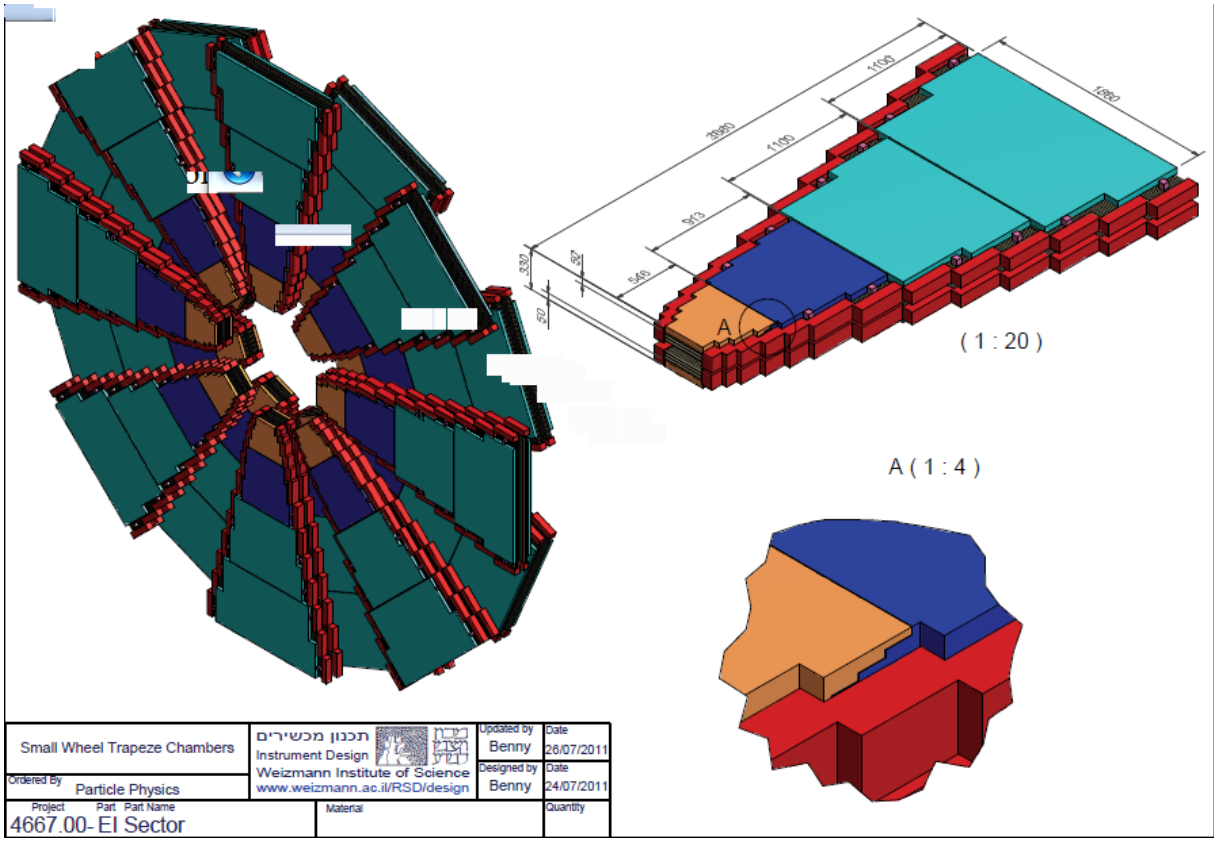

Figure 15: schematic of the detector layout for the case of equal small-large sectors. Insert A shows the stairs-type arrangement for the innermost radial TGC package. The purple boxes represent the alignment elements for the MDT detectors.

Such a layout should be consider as schematic and correspond to one of the possible arrangements of identical small-large sectors. The 8-layer small tube MDT are sandwiched between two TGC packages (each with 5cm thickness) containing 4 gas-gap each; each gas-gap with pad-strip and wire readout. Since the Trigger chambers do not need an overlap region for relative alignment, that part of the MDT surface is used to implement the alignment connection (purple boxes) to the projective alignment bars. The internal structure of each TGC package is the same as that shown in Fig. 13. The innermost radial TGC package are subdivided into two stairs like packages (to provide full coverage in 3 out of 4 layers), in order to keep short wires in the high background region (the readout of the wires is done as an OR of the segments, flagged by the corresponding pad coincidence). The preliminary dimensions of each TGC package can be seen in Fig. 15. This corresponds to a total 192 packages, each of them containing 4 gas-gaps, corresponding to a total of 768 gas-gaps.

The corresponding number of electronics channels is given in Table 5, where the pad surfaces increases from 7.5X7.5cm^2 to 20X20cm^2 at the outermost radial layers. The surface of the pads are determined by the corresponding background rates. The pads would be shifted every two layers (see 16)

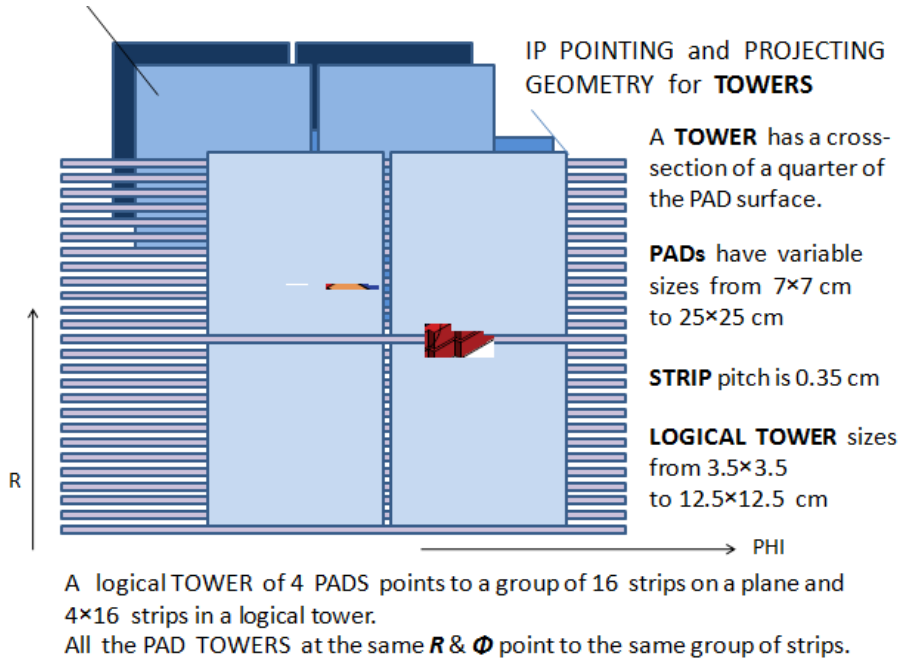

Figure 16: schematics of Pad and strips arrangement (only 2 layers shown).

to reduce the size of the corresponding Region-of-Interest (ROI), from which the strips (wires) will be digitized and used for trigger.

The internal alignment achieved by the production of the strip patterns in the TGC gas gap is precise to within less than 50μm, however the transfer of this precision from gap-to-gap has only been achieved to within better than 150μm. For this reason, the final precision alignment between gaps will be done using tracks from the sandwiched MDT. This requires very few tracks, since the internal strip pattern within a gap is extremely precise.

The mechanical stability of a TGC package is very good for vertically mounted detectors, based on the ATLAS experience. The use of composite materials allows for very small sensitivity to temperatures (in particular within the range of the temperatures in the small wheel), as well as no sensitivity to the magnetic field in the Small Wheel region. To be able to achieve this lack of sensitivity, the mounting needs to be kinematic (one fix point, one sliding point and one plane), of the same type as presently used in ATLAS.

Each package will be connected to 4 HV lines, 3 LV lines and the corresponding optical fibers to transmit the trigger/data information. The HV lines will be connected to one corner of the chamber, while the LV and fibers will be connected to a trigger box, where the logic will be installed. In case of a major failure, the full TGC-MDT-TGC package will be replaced. This will mean that 2 such spare packages for each of the station types need to be constructed.

Component	Number of channels
Strips / side	135,000
Pads / side	30,000
Wires / side	27,500
For two sides detector	385,000

Table 5: channel distribution for the 3 readouts for the 192 packages containing 768 gas gaps.

6.2 Performance

The most important issue for a detector that needs to operate at high rate during a period of more than 10 years, is its aging characteristics. For this reason, a series of small TGCs ($10X10cm^2$) detectors were constructed and exposed to γ irradiation for various periods of time. No deterioration was observed in any of these prototypes, while the one that had the longest exposure was open after a total irradiation of 6Coulomb/cm of wire (i.e. $33Coulomb/cm^2$). Fig. 17 shows the rate and current behavior of the detector during the irradiation. No noticeable degradation is observed after the MIP dose equivalent to 2,000 days of operation at the hottest place in the ATLAS Small Wheel.

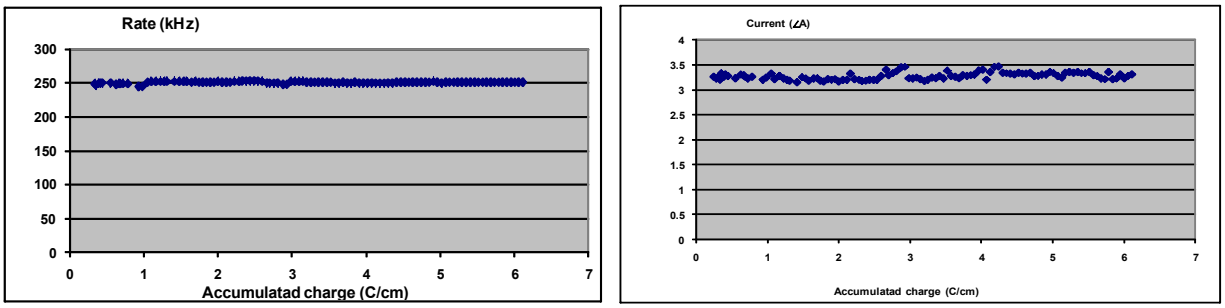

Figure 17: Counting rate and current as a function of the integrated charged in the detector.

The irradiated detector was then open to see the effect of the irradiation. Fig. 18 shows a microscope picture of a wire in the irradiated region, as well as in the non-irradiated region. The deposits in the irradiated region were analyzed and the result of the analysis are shown in the same figure. The deposits being mainly Carbon and Oxygen, as expected from the gas composition.

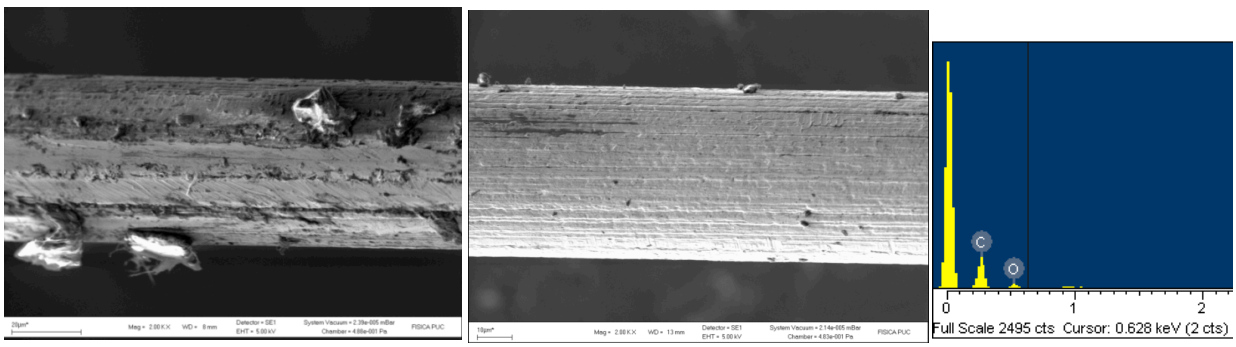

Figure 18: Deposits observed in the irradiated (left) and non-irradiated (center) as well as the e-microscope analysis of the deposits (right).

In order to perform the R&D needed for the use of TGCs in the ATLAS Small Wheels, six large (ranging from 120X100cm^2 to 70X40cm^2) packages of TGCs, each one containing four gas-gaps, each gap with pads-strips and wire readout, have been constructed. These detectors were irradiated in various facilities to evaluate their behavior and position resolution. The time, position and angular resolutions were determined from measurements performed in the H8 facility at CERN, while the efficiency for MIPs under a high full area irradiation with γs was performed at the SOREQ Nuclear Center (Israel) using Co(60) source, while triggering on cosmic MUONs. The sensitivity to neutrons was measured at the Demokritos Nuclear Center (Greece). To simulate the present proposal, the trigger used at the H8 test-beam was the expected 3-out-4 coincidence of pads. The time resolution of this trigger with respect to a beam-defined scintillator is shown in Fig. 19 in units of 0.8ns. It can be seen that the time resolution of the system is consistent with providing the bunch crossing identification with a very high efficiency.

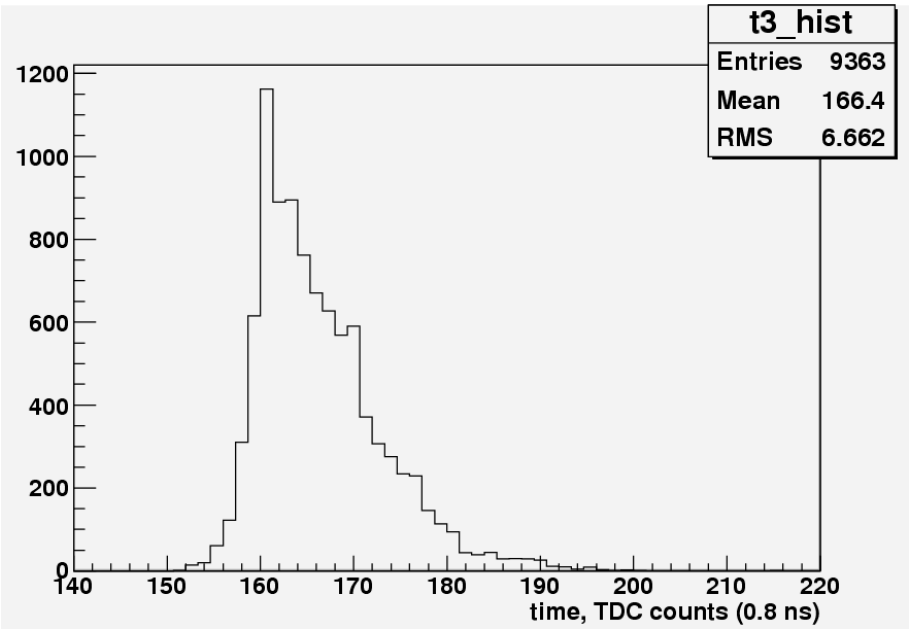

Figure 19: Time difference between 3-out-4 pad trigger with respect to beam scintillator in units of 0.8ns (99% of the distribution is within 25ns).

Fig. 20 shows the individual efficiencies of each of the layers for Pads, Strips and wires of one such package, using the Time-over-Threshold method. It can be see that they are all fully efficient at an operating voltage of 2.9KVolts, which was used for the rest of the tests.

The position resolution of each individual gap was measured by using clean MUON tracks in the small tube MDT test detector that was part of the test beam set-up. The strip multiplicity distribution that provides the charge centroid is shown in Fig. 21.

The obtained position resolution that was calculated by making a fit to the difference between the layer being measured with respect to the position calculated from a fit to the other three TGC gas gaps is shown in Table 6 (before and after the correction for inter-gap misalignment), while a typical distribution is shown in Fig. 22. It can be seen that the individual position resolutions are consistent with the needs of the Small Wheel and provide a very good complement to the MDT measurements.

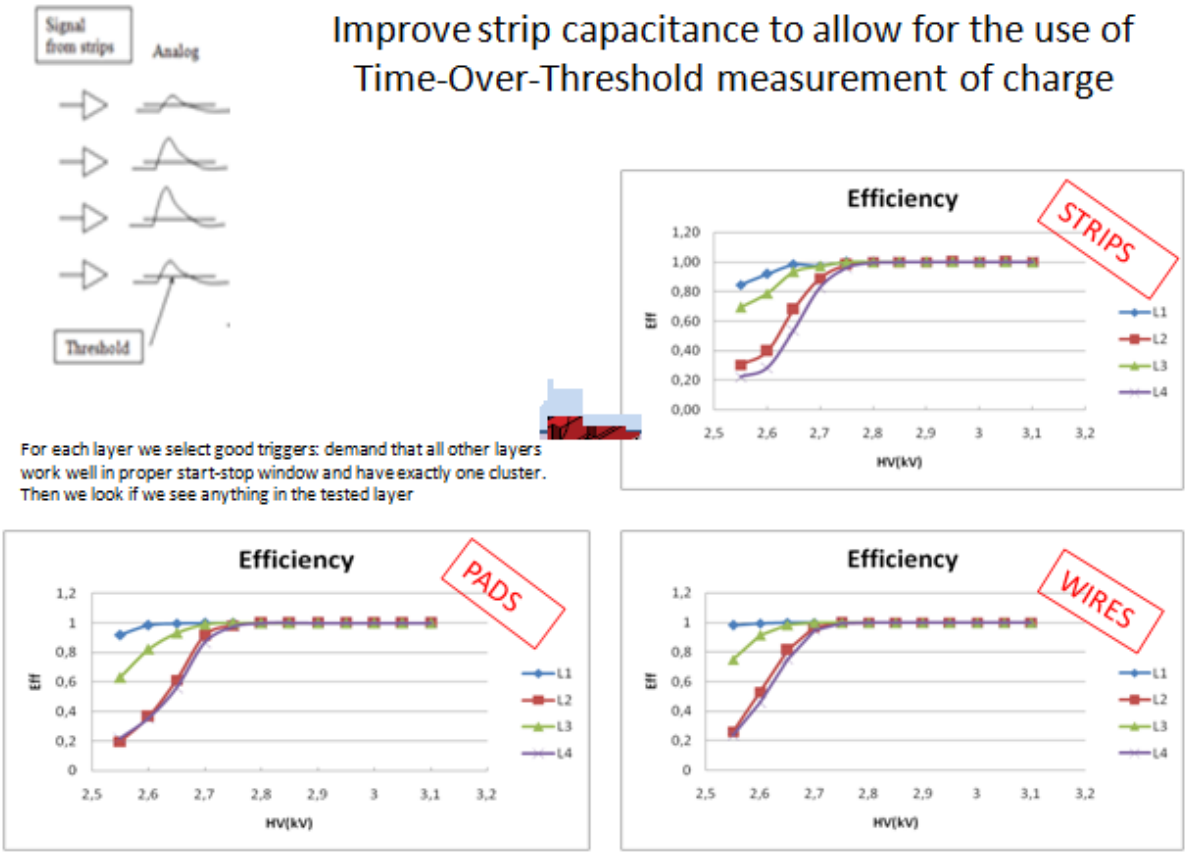

Figure 20: Plateau curve for each of the gaps used in the test, using the T-O-T method.

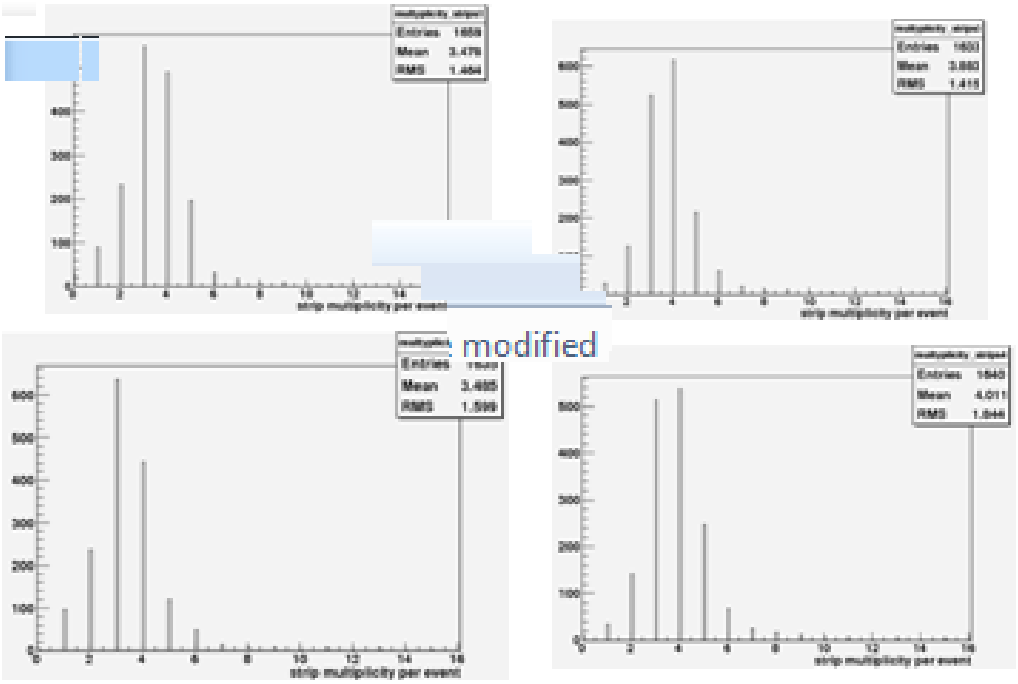

Figure 21: strip multiplicity for a MIP on each of the individual gas gaps.

The position resolution as a function of incident angle has been measured in the past using a regular ADC to determine the charge in each individual strip (the measurement to be repeated

Layer	$\sigma_{corr}(\sigma_{nocorr}) \pm \Delta\sigma[\mu\text{m}]$
1 new	66.2 (120.9) ± 1.2
2 new	66.7 (79.8) ± 1.1
3 new	63.6 (76.0) ± 1.0
4 new	63.8 (116.49) ± 1.0

Table 6: position resolution obtained for each layer after (before) correcting for individual layer position.

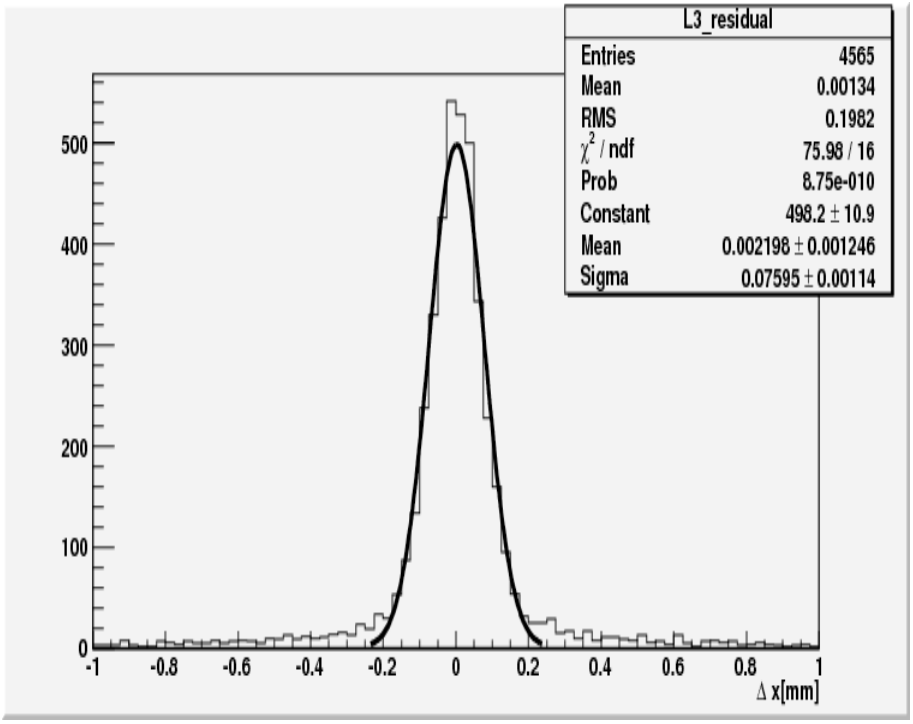

Figure 22: Typical residual for one of the layers with respect to the fitted line.

in the forthcoming August 2011 test beam using Time-over-Threshold). The dependence of the single layer resolution as a function of angle is shown in Fig. 23.

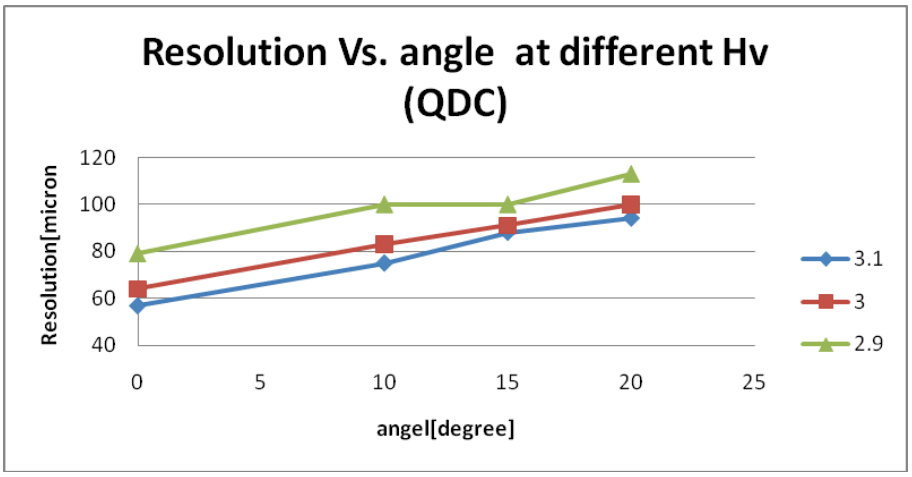

Figure 23: Resolution vs incident angle as measured with MUONs in H8.

The angular resolution of a single TGC package was obtained by comparing the angle between one package of TGCs (4 gaps) with that measured with the small tube MDT test chamber. The difference has a resolution of 3mrad. Having such a resolution with a single TGC package (5cm thick) implies that with two packages separated by 300mm, the angular resolution of the system would be better than 03mrad at the Level 1 trigger. Finally the measured single layer efficiencies for MIPs in a γ background has been measured by triggering with cosmics under a high irradiation flux. The results are shown in Fig. 24. Similarly, this was done with 5.5MeV neutrons. The corresponding single layer efficiency is shown in Fig. 25.

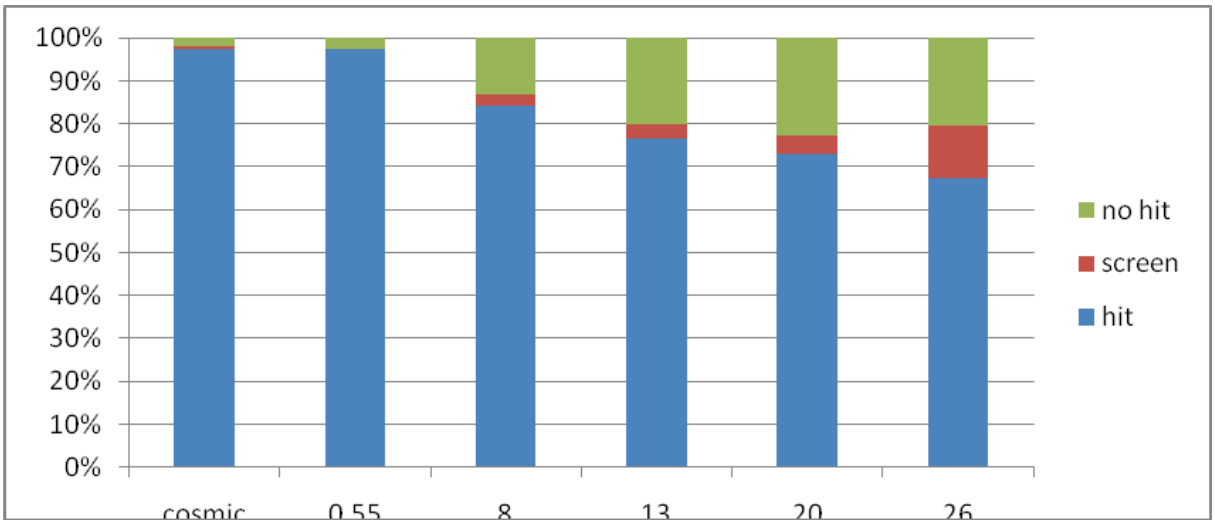

Figure 24: Single layer efficiency in k/Hz per cm^2 on a large chamber under uniform irradiation (strips length= 1.2m).

Figure 25: Single layer efficiency for MIPs under 5.5MeV neutron irradiation.

Finally, by using the Time-over Threshold method, one can easily reject single gas-gaps measurements that have been polluted by either a δ-ray, a γ or a neutron, by demanding less

than six strips in a cluster and a cut on the Time-over-Threshold. This is illustrated in Fig. 26, where one can see the passage of a MUON through the four gas-gaps, without contamination, while the other event displays show one layer with a δ-ray and with a neutron impinging in the same region.

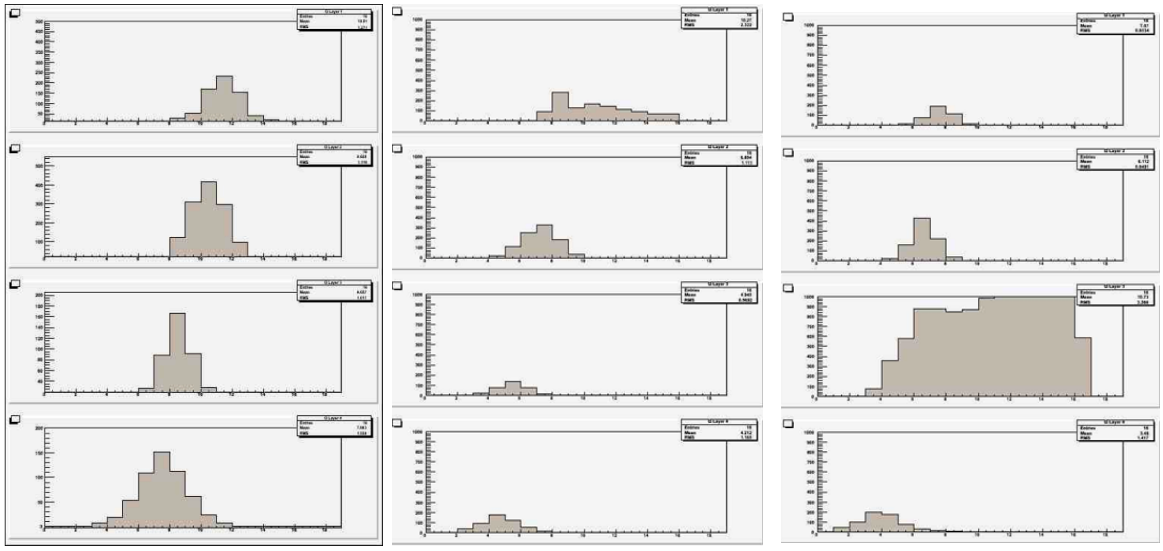

Figure 26: Event display of a) a clean MUON track, b) a MUON track with a δ-ray in the first the gas-gaps and c) a neutron interacting interacting in the 3^{rd} gas gap, during the neutron tests at Demokritos.

6.3 L1 trigger and electronics

1. *Production of L1 signal starting from the detector signal till the formation of SL input.*

   comment Here we will show a diagram showing the two packages with the MDT in between.

   The small wheels strip signals are used to extrapolate a track to the Big Wheel where the Sector Logic corroborates it with the existing 2-out-of-3 and 3-out-of-4 coincidences in the Big Wheel chambers. The fine granularity of this extrapolation gives the high trigger rejection. The logic added to accomplish this must not cause the latency to the Sector Logic input to exceed 1.05 microseconds (See Table 8). The sub-sector of the extrapolated muon is found as follows: In the Small Wheel chambers, a local trigger is made from two 3-out-4 coincidences in a tower of pads made from the 8 layers of detectors. (Alternating layers have their pads shifted by half a pad in both dimensions to give x4 granularity logical towers.) The triggering tower selects all the strips on all layers that pass through that logical tower. The signals from these strips are selected and switched into 8 centroid finders, one per layer. This selection makes a 20-fold reduction in the number of strips that must be processed as well as the number of centroid finders. The four centroids in each 4-gap sTGC package are averaged to give a point in 3-D space. The two points thus found and the difference in their z-coordinate define a vector which, when extrapolated to the Big Wheels by means of a look-up table, define a sub-sector (in η, ϕ) of the Big Wheels. The high precision in radius of the two centroids provides an angular accuracy better than 0.3 mrad. A block diagram of the trigger logic is shown in Figure 14, as

implemented for a demonstrator. Each pair of chamber packages has its dedicated trigger logic. Centroid finder details:

- The centroid finder currently calculates the centroid from the charge on five strips.
- The charge on each strip is approximated by measuring the time-over-threshold, currently with 1 nsec steps and 8-bit dynamic range. This will depend on the final ASD characteristics.
- Centroids are included in the average only if the number of strips above a threshold is not too large – due to, for example, a delta ray.
- To compensate for differences in signal routing and particle time-of-flight, strip signals can be delayed in steps of 1 nsec, up to 25 nsec, with 16 strips sharing a delay parameter.

ASD

The baseline is to use BNLs VMM Front End chip, now under development, that includes both an ASD and readout logic. The planned parameters of this chip (see table) match the needs of the sTGC detectors. The first prototype chips of the Front End will be available at the end of 2011. The sTGC version of this ASD has LVDS outputs suitable for the time-over-threshold trigger logic.

Split into on-chamber and off chamber logic

We seek to minimize the amount of on-chamber electronics because access and power is limited and on-chamber electronics must be radiation tolerant, and therefore probably in ASICs as opposed to reprogrammable FPGAs. The row selector, driven by the pad tower coincidence, reduces the number of channels to be passed to the off-chamber electronics by a factor of about 20. This selector and the pad coincidence must clearly be on chamber. The channel delays depend on the channel, so they must be before the selector. If the Time-over-Threshold logic is done on-chamber, the bandwidth needed between on and off chamber electronics is much reduced, since 100 bits of 1ns signal samples are reduced to an 8-bit time-over-threshold. However the radiation tolerant ASICS must be more complex. If placed off-chamber, more bandwidth, i.e. links and fibers, and probably serializer power, is needed, but the radiation tolerant electronics is simpler. The final decision on this optimization will be taken when details of radiation tolerant ASICs and of serializer speeds and power are better known. The centroid finding through calculation of the Big Wheel sub-sector will be done in off-chamber FPGAs.

2. *Latency (calculation, measurement with demonstrator)*

   See Table. 8.

3. *Compatibility with Phase II upgrade*

   The pipelines and derandomizers will be designed to handle a 500 kHz Level-1 trigger rate and to accommodate up to 10μs Level-1 latency.

6.4 Readout electronics and integration in DAQ

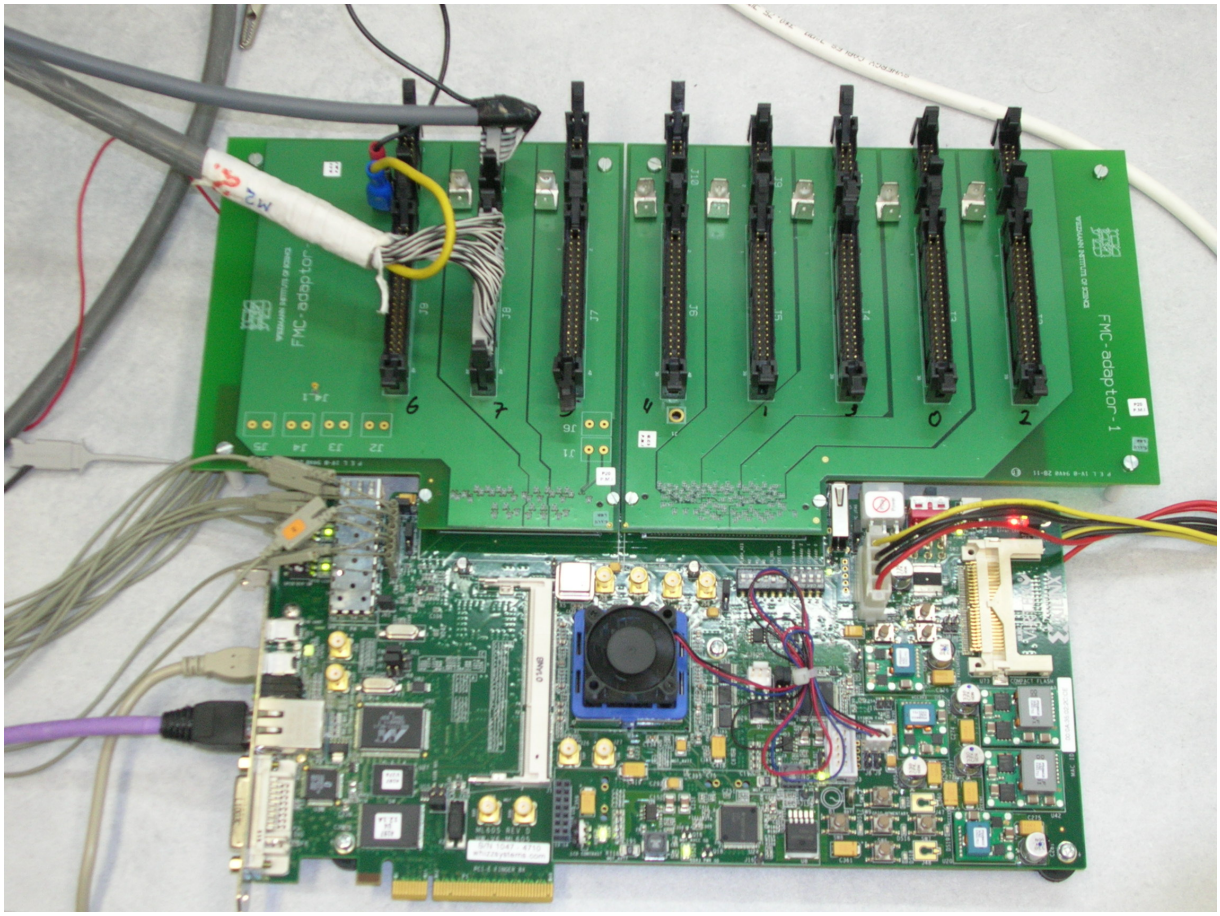

Figure 27: The trigger demonstrator board based on a commercial evaluation board.

Date	Name		
August 2011	Demo-0	Goal	Demonstrate total latency, ASD to Sector Logic input, of pad local trigger, strip selection and sub-sector calculation from centroids in an FPGA.
		Includes	KEK TGC ASDs and Carioca ASDs, 4 layers of 16 strips, 4 layers of 8 or 14 pads, simple non-pipelined readout, based on commercial FPGA eval board
		Excludes	links and fibers, pipelined readout, rad tol technolgy
December 2011	Demo-1	Goal	Add channels to do full 8-layer logic, 64 strips per layer
		Includes	based on purpose built FPGA board
		Excludes	pipelined readout, rad tol technology
February 2012	Demo-1a	Goal	Run with BNL VMM Front End chip (ASD only)
Early 2012			Define on-chamber/off chamber split and choose link hardware.
			Design on-chamber boards
			produce rad tol ASICs for on-chamber part
			2nd spin of rad tol ASICs
			design off-chamber boards
			production of on- and off-chamber boards

Table 7: sTGC trigger development schedule

	Min (ns)	Max (ns)	notes
TOF from interaction point to SW (10 m)	35	35	
Propagation delay in chamber	25	25	
ASD	10	10	
On chamber cabling (1.5-2.5m) to selector	8	13	5nsec/m
up- to down-stream package (50cm)	0	3	
delay for pad trigger and deskew	15	25	
selector	5	10	switch
serializer	5	10	
deserializer	8	16	
Run Length Encoder	16	24	
latency for the last sample of the pulse	64	100	depends on shaping time
find largest signal	7.5	15	
centroid of a layer	13	25	8 layers done in parallel
centroid chooser	5	10	
centroid average	8	15	
tracklet calc (LUT)	8	10	datasheet BRAM access time =2nsec
output serializer	50	75	GBT: 3 clocks
fiber to Sector logic 90m	495	495	5.5nsec/m
	776	**916**	

Table 8: Latency calculation - The table shows the latency with the insertion of the precision strip trigger logic into the existing path from the Inner Layer coincidence logic to the Sector Logic. We take as a model the Xilinx Virtex6. All numbers are estimates except that for the centroid finder for which a realistic design has been simulated.

6.5 Services, infrastructure, and DCS

1. Gas system and distribution The gas system is a natural extension of the present TGC gas system, which will be extended from the present eight manifolds (four for EIL4 TGCs and four for the SW TGC chambers) to one containing 20 manifolds (four for the EIL4 chambers and 16 for the new Small Wheel chambers (one/layer for the upper and similarly for the lower chambers). This will be less than the normal manifolds in the Big-Wheels and can be easily be added to the present SW racks. The manifolds will be running at a flow rate of 40l/hr of the regular TGC gas mixture, which corresponds to a volume exchange every four hrs. The extra flow corresponds to a 25% increase to the present TGC gas flow, which can be implemented in the present gas system, without any additional modifications, except the extra flowmeters in the present SW racks. The safety system for the new detectors will be the same as for the present one, that were approved by TIS.

2. Integration in DCS system, requirements for DCS

   - Chamber charge monitor
   - HV control and monitoring, trip recovery
   - LV power control and monitoring
   - Temperature monitoring
   - Link health statistics

- ASD configuration parameters (threshold, peaking time, etc.)
- Front End trigger and readout configuration parameters (delays, channel masks, pipeline depth, etc.)

7 Detector concept 2 : MDT + RPC (working title)

We propose here a dedicated trigger detector based on enhanced version of the avalanche RPCs to complement a precision tracking small tube MDT (sMDT) system in view of the SW upgrade. The choice of the RPCs as trigger detector is motivated by the extreme simplicity and robustness of this detector and even more by its excellent timing capability that, as it will be shown in this report, is crucial to reject low energy uncorrelated background in an hostile working environment. On the other hand the idea to combine a precision tracking detector with a dedicated trigger detector extends to the SW upgrade a concept that has been successfully applied to the whole muon system of ATLAS. The relatively cheap construction, the possibility of being tailored to any shape and the small amount of space it occupies, and recent breakthrough in the RPC front end allowing a great increase of the rate capability, makes the RPC detector attractive for the ATLAS SW upgrade. Moreover a substantial improvement with respect to the present muon system will be a full MDT-RPC integration concerning the mechanical structure, the electric services and the DAQ that will be based on similar ADC and TDC circuits as developed in the present MDT mezzanine cards.

List of participating Institutes The Institutes which so far have expressed interest for this project and are participating to the preparation of the present document are:

- Argonne National Laboratory
- Istituto Nazionale Fisica Nucleare Sez. Bologna (to be confirmed)
- Boston University (possible participation)
- University of Michigan
- University of Science and Technology of China
- Academia Sinica, Taiwan
- University of Roma and INFN Tor Vergata
- University of Washington

7.1 Detector technology and layout

1. **Description of detector concept** Figure 28 shows the layout of the SW detector with sMDTs as precision tracking chambers and RPCs as trigger chambers. The difference between the two angles measured by the new small wheel detector and the current EM TGCs will be used to determine the muon momentum at L1. The RPC (or mRPC as will be specified later) will be assembled together with a sMDT of equal dimensions in a common mechanical support structure which guarantees the relative alignment of the RPC to the rest muon sub-detectors in the endcap region. In order to reach the designed momentum resolution at L1, the angular resolution provided by the new small wheel detector should be about 1 mrad.

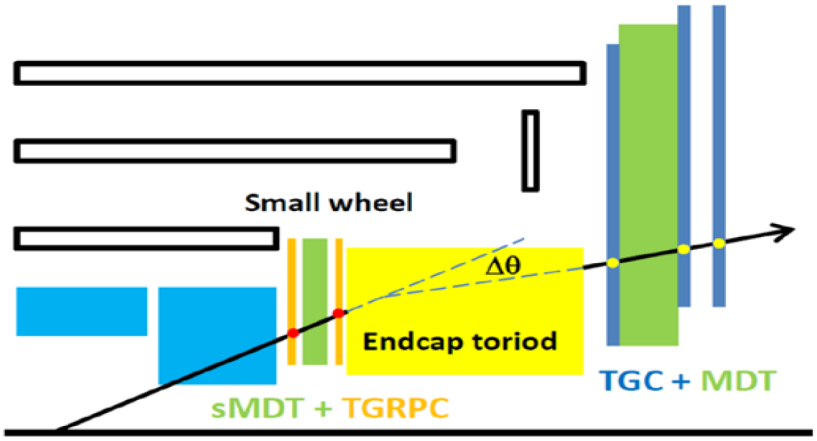

Figure 28: Detector layout for the small wheel upgrade using sMDT as the precision tracking chamber and thin gap RPC as the trigger chamber.

In order to fulfill the requirements defined for the SW upgrade, a substantial improvement with respect to the RPCs presently operating in ATLAS is needed concerning the rate capability, time resolution, position resolution and detector ageing. The ATLAS RPCs were successfully tested at a rate of 1 kHz/cm^2 and were qualified, following the ATLAS requirements, for ageing effects equivalent to 10 years operation at a rate of 100 Hz/cm^2, corresponding to 0.3 C/cm^2 integrated charge. Although larger values are acceptable for the integrated charge, we stress here that the best way to increase the RPC rate capability is to reduce the charge delivered per detected avalanche, rather than to increase the operating current using very low resistivity electrode plates [ref]. Operation at low current is indeed crucial to decrease the detector ageing and the power dissipation. For this purpose two parameters have to be optimized: the gas gap width which determines the amount of delivered charge per avalanche and the sensitivity of front end electronics which determines the minimum charge that can be discriminated from the noise.

Fast detectors are crucial to reject low energy uncorrelated background. At rates as high as 10 kHz/cm^2, a very short time (about 2 ns) coincidence between contiguous detectors is an extremely efficient method to eliminate uncorrelated hits. This requires to improve the time resolution to $0.3 - 0.5$ ns. A thinner gap RPC would fulfill at the same time both requirements: to reduce the delivered charge and to improve the time resolution. We propose here to split the standard 2 mm gas gap of the ATLAS RPCs in two gaps of about 1 mm.

The charge centroid method applied to the RPCs allows to obtain a space resolution of the order of 0.1 mm on both coordinates. However the time required by the DAQ and the centroid computation would be too long for a 1st level trigger. We propose therefore to use narrow strips, with typical pitch of about 2 mm, coupled to a maximum selector circuit that should give the centroid position within 0.3 mm.

The RPC is a gaseous parallel electrode-plate detector whose working principle has been already described in detail [ref]. The Atlas RPCs presently working in the barrel are based on a 2 mm gas gap between two resistive electrodes 2 mm thick, made of a melamine coated phenolic laminate that is usually (and improperly) referred to as bakelite. The gas volume just described is sandwiched between two read out panels with mutually orthogonal strips giving a point in the space for each avalanche generated inside the

gas. The low p_T stations are made of two RPC doublets, with the MDTs in the middle, and giving 4 points along the muon track with a trigger logics requiring a 3 out of 4 coincidence.

The scheme we propose for the SW upgrade is conceptually very similar to that just described, with the following differences required by the more difficult working conditions with respect to the barrel.

- The single 2 mm gas gap is split into two 1 mm gaps giving the advantages of a better time resolution, a lower delivered charge which increases the rate capability and a higher efficiency due to two gaps inducing simultaneous signals on the same strips. We will refer to this type of RPC as mRPC for its double (multiple) gap.
- The electrode thickness is reduced to 1 mm not to increase the average distance of the avalanches generated in the gas from the pick up strips in a two gaps structure.
- The two doublets structure is improved to two triplets (Fig. 29). This allows to make very short time coincidences among detector layers of the same triplet, thus strongly reducing the uncorrelated background. The trigger logics requires the 2 out of 3 coincidence inside the same triplet followed by the twofold coincidence of the two triplets signals.
- The eta strips width is strongly reduced to improve the angular resolution in the bending view. Typically a 2 mm strip pitch is foreseen. The thin strips are grouped in super-strips 12 mm wide connected to a maximum selector which identifies, in a typical time of 10 ns, the mini-strip of maximum charge, which gives the best position for the track.
- The strips of at least one of the two views will be equipped with both ends read out connected to a mean-timer circuit. This will improve the trigger performance for two fundamental reasons:
  (a) The track position will be localized along the strip with a typical uncertainty of a few cm giving a further reduction of uncorrelated background in the coincidence of two contiguous chambers;
  (b) In case of two or more muons crossing the same chamber the simultaneous measurement of both coordinates on the same strip will remove ambiguities and ghost hits.
- A further fundamental concept of this proposal is the idea to substantially increase the front-end electronics sensitivity and signal to noise ratio, and to reduce consequently the required gas gain amplification. The low gas gain operation is indeed of crucial importance to increase the rate capability without increasing at the same time the power dissipated inside the gas and the ageing of the detector. Test of RPCs equipped with a new front-end circuit [ref] have shown that a factor of at least 7 in terms of total charge delivered in the gas, and thus in rate capability, can be achieved.

Our baseline proposal is based on a triplet of 1+1 mm bi-gap mRPCs. Figure 30 shows two possible configuration of the bi-gap being considered, the topmost is the classic mRPC configuration with a floating central electrode; below is shown a bi-gap made essentially of two electrically independent single gap detectors being read externally by the same readout strip planes. However the overall project is aimed to optimize rate capability,

background rejection, mechanical robustness and number of read out channels. This many parameter optimization requires accurate simulations that are not yet been made. We are therefore keeping on study other possible configurations.

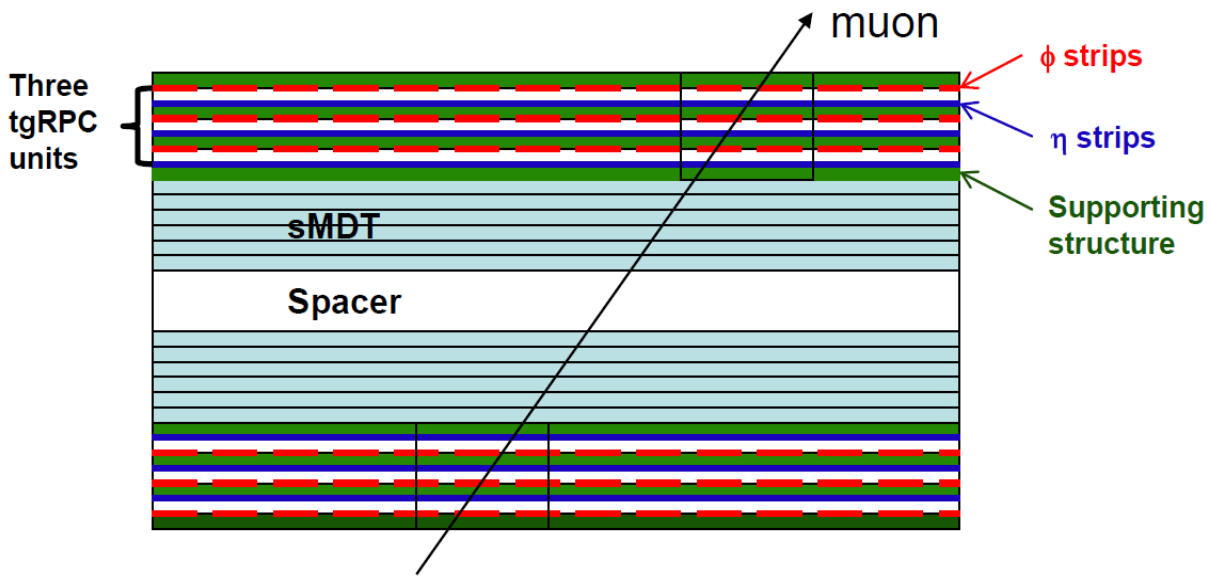

Figure 29: Layout of the mRPC detector with three units on both sides of the sMDT chamber. Each mRPC unit will be read out along both eta and phi directions.

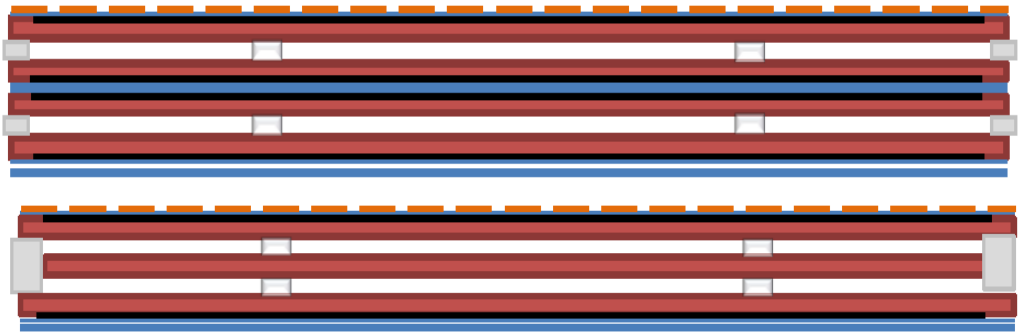

Figure 30: Two possible configurations for each mRPC detector. Top: classic multi-gap configuration with the inner floating electrode; Bottom: a bi-gap made of independent single gap detectors. Each mRPC will be read out along both eta and phi directions.

2. **List of all operating parameters**

   Table 9 summarize the present baseline chamber parameters. Further parameter fine tuning is under study so this numbers are suitable to change. The detector structure inherits most features (except thickness) from ATLAS experience. Readout strips along eta and phi directions are placed on the outer surface of the bakelite electrode plates. All plates have a thickness of 1 mm and a volume resistivity of $\sim 10^{10}$ Ω cm. The gas gap size is 1mm, and the correct distance between two plates being assured by a grid of spacers. Graphite layers with surface resistivity of 100 kΩ, transparent to the fast RPC signal, are painted on the external surfaces of resistive plates, to distribute the high voltage. A 100 μm insulating foil of PET separates the graphite electrodes from the readout.

Parameter	Design value
Operation mode	Avalanche
Timing resolution	<0.5 ns
Rate capability	10 kHz/cm^2
Gas gap	1 mm
Bakelite plate thickness	1 mm
Bakelite resistivity	$\sim 10^{10}\Omega$ cm
Prompt Eta-hit position resolution	0.3 mm
Prompt Phi-hit position resolution	3 mm
Off line Phi-hit position resolution	0.3 mm
Eta-strip pitch size	2 mm
Phi-strip pitch size	0.8 - 2 cm
Gas mixture	$C_2H_2F_4$/ Iso-C_4H_{10}/SF_6 (94.7/5.0/0.3)
Operating voltage	$\sim$ 6 kV (12 kV for the floating electrode bi-gap version)

Table 9: Parameters for the mRPCs. All the values are still to be considered as approximate

The high voltage to be applied to each gas gap is $\sim$ 6 kV allowing the RPC running with a low gain avalanche mode enhancing the detector rate capability. The gas mixture of C2H2F4/Iso-C4H10/SF6 (94.7/5/0.3) used by the current ATLAS barrel RPCs is also expected to be used for the proposed mRPC detector.

The detector layers are interleaved with two support panels made of light-weight paper honeycomb and are held in position by a solid frame of aluminum profiles. The total thickness of a mRPC unit with bakelite plates and gas gap readout PCB board is about 10 mm thus the triplet can easily fit the tight space budget for the SW upgrade, including some support structure. Further optimization is under study for the integration of the RPC and MDT chambers in a hybrid single piece of detector.

The main operating parameters for the proposed mRPC detector are given in Table 9.

3. **Detailed layout: acceptance, description of chamber overlap and dead areas, drawings**

   The layout of the mRPC detector will follow the layout of the sMDT system with large and small sectors. The layout of the large and small sectors of the new small wheel can be found in Fig. 31. The mRPCs we propose will cover the pseudorapidity range of $1.05 < |\eta| < 2.7$ and be mounted on both sides of the sMDT chambers with readout strip position referenced to the sMDT tubes for internal alignment. The azimuthal angle coverage is 100% due to the overlap of the small and large sectors.

4. **Tables with chambers sizes, number of channels**

   In total, there will be six types of mRPC chambers with different sizes, three for big sectors and three for small sectors. There will be 48 chambers in total for each wheel. All chambers have a trapezoidal geometry, and the covered area ranges from 0.9 m $\times$ 1.1 m to 2.0 m $\times$ 1.5 m for large sectors and from 0.8 m $\times$ 1.0 m to 1.6 m $\times$ 1.1 m for small sectors. Details can be found in Table 11 and 10.

   With an eta-strip readout pitch of 2 mm and readout from both ends, the total number of readout channels is estimated to be 225.4 k for both wheels. The total number of readout

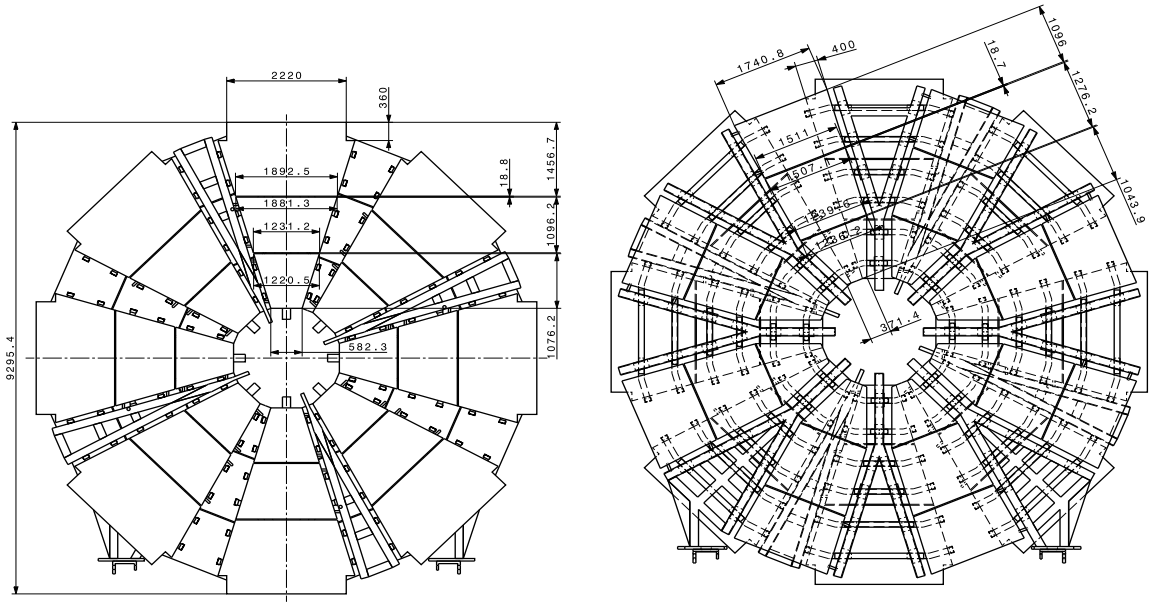

Figure 31: Layout of large (left) and small (right) sectors.

channels is calculated using the sum of readout channels in Table 2 multiplied by 8 for eight sectors (both large and small sectors) and 2 for wheels on A and C sides.

5. **Internal alignment scheme (the overall common endcap alignment scheme is described in the previous chapter)**

   A mRPC will be glued on the surface of a sMDT chamber with similar dimensions. The relative position of the mRPC to the sMDT is expected to be within 50 microns. The internal alignment of the RPC depends on the precision of the readout strips on the PCB. A strip position precision of 25 microns (???) for readout strips on a PCB is expected.

6. **Calculations about mechanical stability and expected deformations due to**

Chamber type	η channels per chamber	ϕ channels per chamber	Total channels per wheel	Total Power per wheel (W)
Big sector, type I	3240	1500	37920	758
Big sector, type II	3240	1500	37920	758
Big sector, type III	4320	1500	46560	931
Small sector, type I	3240	1200	35520	710
Small sector, type II	3960	1200	41280	826
Small sector, type III	3240	1200	35520	710
Total per wheel	21240	8100	234720	4694

Table 10: Channels and power statistics for six types of mRPC chambers and for the whole New Small Wheel.

Chamber type	Chamber geometry (top/bottom/height) (mm)	Num of layers × chambers	Phi pitch (mm)
EIL0	2400/1892.5/1456.7	3 × 2	20
EIL1	1881.3/1231.2/1096.2	3 × 2	14
EIL2	1220.5/582.3/11076.2	3 × 2	8
EIS0	1740.8/1511.0/1096	3 × 2	20
EIS1	1507.1/1239.6/1276.2	3 × 2	14
EIS2	1236.2/371.4/1043.9	3 × 2	8

Table 11: Detector dimensions for six types of tgRPC chambers and the corresponding number of readout channels per sMDT-tgRPC unit. The factor of 4 counts for readout from both ends and two doublets on a sMDT chamber.

gravity, temperature changes, (magnetic field) etc.

Since the mRPC will be directly integrated on the surface of a sMDT, the flatness and the mechanical stability should be similar as the sMDT chambers. The mRPCs have small size and will be installed vertically, the gravity effect will be negligible. The temperature and magnetic field effects should be small and will be monitored by the MDT temperature and magnetic field monitoring system.

7. **Requirements for mount points**

   The mount points are on sMDT chambers and no mount points are needed for mRPC.

8. **Details of service points and other positions where access is needed**

   Each sector will have one gas inlet and one gas outlet with fanout/fanin to each chamber. High voltage for each sector will be applied through high voltage splitting boxes similar as used for the current MDT system.

9. **Concept for chamber replacement (what needs to be dismounted etc.)**

   The whole sMDT-mRPC unit needs to be dismounted if we need to replace either the sMDT or the mRPC.

7.2 Performance

In this section firstly is described the performance and features of the single RPC detector element. Basing on this the features of the proposed RPC based subsystem will be analyzed.

7.2.1 The single gap RPC intrinsic performance

The RPC sensitive volume is a thin layer of gas confined between parallel resistive electrodes, establishing an uniform field in it and allowing a prompt signal production. The fast electron avalanche signal can be read by means of external electrodes on which a 2D charge distribution is induced by the growing avalanche.

The 2D charge distribution has an approximate gaussian shape whose width is essentially dependent on the gas gap and electrodes thickness [**?**] [**?**]. For instance for an ATLAS standard RPC (2 mm gas gap and 2 mm electrodes thickness) the FWHM of the charge distribution is about 6 mm as shown in fig.**??**. An enhanced layout of 1 mm gas gap and 1 mm thick electrodes will produce a charge distribution with halved width. The impact point of the particle is localized on the transverse plane though the position the charge distribution maximum, within a few hundreds of microns in each direction, depending on the detector layout. In a recent test a resolution of $\sim 300\ \mu m$ has been measured at the H8 test beam with a non optimal 13 mm pitch strip readout panel **??**, using the charge centroid method.

Has been shown that the 2 mm gas gap have a time resolution of ~ 1 ns and has been demonstrated that this enhances inversely with the gap width [**?**, **?**]. In figure **??** the signal development for different gap width is compared. For 1 mm gas gaps a time resolution of about 0.5 ns is expected

The gas gap intrinsic efficiency, thus the ability of producing a detectable avalanche, depends essentially on the primary ionization statistics of the incident particle on the gaseous target. The ionization density of a MIP for the ATLAS gas mixture is about 15 couples/mm. Being the first fraction of the available gas target suitable for an efficient avalanche detection, the inefficiency is still negligible for 1 or 2 mm gas gaps while some efficiency loss is visible for a 0.5 mm gas gap as clearly visible in fig. **??**. A fixed inefficiency contribution of about 1% has to be considered due to spacers and frames. The gas gain depends on the applied field and its fluctuations are dominated by the initial position of the very firsts electron/ion couples. Due to the space charge saturation effects the charge tend to grow linearly with the drift space [**?**], producing a compression in the charge distribution dynamics and a peaked shape.

The avalanche detection has to do with the signal to noise ratio of the ensemble constituted by the RPC and its readout system, thus it cannot be disentangled from the front end amplifier design and performance: The higher is the performance of the last the lower is the gain requested in the gas for a given efficiency. This has an obvious consequence on the detector rate capability and ageing performance. A newly developed frontend amplifier applied to an ATLAS like RPC permitted a substantially lower working point corresponding to a factor of 10 less charge delivered per count. A test performed at the CERN GIF with this frontend demonstrated a full efficiency detection for triggered cosmic rays while counting 8 KHz/cm^2 of photons illuminating the whole chamber surface (fig. **??**).

The response of an RPC to large ionization events is determined by two facts: The saturated avalanche operating mode and the resistive electrodes. The saturated avalanche growth, as described in [**?**], is linear with increase of drift space or electric field until the limit for generating a streamer is reached. Similarly a fluctuations of the primary ionization has a slight effect on the total charge. This mechanism is making extremely unlikely the generation of a streamer but even in this extremal case the streamer charge is only about a factor of 10 larger than the avalanche and anyhow the bulk resistive electrodes have the fundamental property of self extinguishing the charge multiplication [**?**] due to a local field depletion which is restored slowly with respect to the discharge time constant.

7.2.2 The overall performance of the SW RPC stations

Hereby follows the analysis of the proposed RPC station performance as tracking trigger. The baseline design consists in two RPC chambers sandwiching the sMDT chamber, each chamber being a triplet of 1+1 mm bi-gaps as shown in fig. **??** and described in 7.1. Each gap is readout by orthogonal strip planes. The strip pitch is $\sim$ 1-2 cm in the ϕ coordinate while the bending coordinate η is segmented in strips of 2 mm pitch. All the strips are equipped locally with a newly developed extremely sensitive front end amplifier allowing the RPC signal detection with a factor of 10 less charge delivered in the gas with respect to the present ATLAS RPCs. The full features of this circuit will be described in Section 7.4.

The ϕ strips are readout by means of the same readout cards used for the sMDTs providing 0.3 ns timing and charge readout. The Eta strips are read in groups of 8 (a super-strip) by an especially developed circuit, the Maximum Selector (MS since now), allowing to extract from the charge distribution the strip or the strips having the maximum induced charge. A fast mean-timer circuit (MT since now) has also been developed with a resolution of 250 ps. It will process the signal coming from both ends of a η super-strip allowing to promptly locate the particle impact event in a very narrow space-time region of $\Delta\eta \times \Delta\phi \times \Delta t = 1cm \times 5cm \times 2ns$. Both circuits will be described in Section 7.4. Optionally a solution having the MT placed on the ϕ strips to minimize the channel number is being studied.

The different features performance list:

1. **Spatial and angular resolution as functions of rate and angle of incidence**. The space resolution for orthogonally incident MIPs on a single detector plane:

   - for *phi* strips $\sim$ 1 cm $/\sqrt{12}$ (promptly) and $\sim$ 0.3 mm with off-line calculation the charge centroid
   - for $\eta \sim$ 0.3 mm by means of the maximum selector. This is calculated as follows: $0.5 \cdot strip\_pitch/\sqrt{12}$, where the factor 0.5 is coming from the exploiting of the cluster size 1 and 2

   Given the lever arm of about 40 cm this would already satisfy the angular resolution $<$ 1 mrad. The presence of at least 2 points per RPC chamber further enhances the angular resolution. The final result depends on strip alignment details of the chamber layout which are not yet fixed.

2. **Time resolution** A single 1 mm gas gap has a resolution of about 0.5 ns, which further improves in the 1+1 mm bi-gap configuration since the timing goes with the OR of the two sub-gaps. An exact estimation will be calculated and tested. Further timing enhancement, valuable for TOF applications is provided by the multiple measurements done by the two triplet chambers

3. **Efficiency (single measurement and segment)** With 1 mm gaseous target thickness an efficiency of about 99% can be achieved by the single gas gap. Nonetheless this is not the best in terms of charge per count economy. The multi-gap structure with common readout in facts allow to:

- achieve high efficiency
- limit the charge per count
- minimize the number of channels
- improve the timing

The first two points are determined by the fact that the most of total charge per count delivered is due the the last 10% of efficiency, due to the avalanche growth dynamics. Therefore a big advantage is coming from subdividing the gap in sub-gaps in OR with respect to the delivered signal. Moreover the total delivered charge for a given signal amplitude is 1/N where N is the number of sub-gaps [**?**]. For example operating the single sub-gaps of a bi-gap at 90% of efficiency would result in efficiency ¿99% with a factor of ~ 4 of saved charge per count, by combining the two effects.

A similar logic suggest to implement a 2/3 majority coincidence in each chamber to individuate the muon segments. Each segment is individuated by at least 2 points per chamber. To make an example the failure probability of the single chamber is less than 0.5% for single bi-gap efficiency of 96% (corresponding to a sub-gap efficiency of 80%); the segment failure probability given by the AND of the two chambers is less tan 1%.

4. Double track resolution The double track resolution for the trigger is driven by the maximum selector granularity in η and the strip pitch in ϕ, both of the order of 1-2 cm. The mean-timer readout using the information from both end of one of the strip planes permit to eliminate the ghosts: two real hits on the same detector, read by strip planes on the two coordinates, would give rise to 4 potential hit points at the crossing of each couple of strips. The mean timer eliminates the ambiguity is the hits are more than 5 cm distant in the mean timer coordinate.

5. **Rejection of fake and background tracks** The high level of background is a potential source of fake triggers. This can come by random coincidences of photon hits, largely dominating the background or by a combination of this and low energy charged tracks, which are mostly synchronized with the real tracks and able to trigger at least one of the two chambers. The RPC detector design will exploit the space-time detector performance to minimize this fake contribution. Here follows a simple calculation of fake rate based on the proposed layout more details are given in section 7.3:

   - We assume 10 kHz/cm^2 and the maximum background rate
   - the mean-timer applied to a single mRPC selects an area of $\sim 1.6\times5$ cm^2. Figure 32 shows the benefit of using mean-timer to determine the hit position along the phi strip.
   - The RPC time resolution and the mean-timer allow a $\pm3\sigma$ time window of ~ 3 ns for the 2/3 majority. This produce a chamber fake rate on a 8 cm^2 virtual pad of:

$$(0.8 \cdot 10^5 Hz) \times (7.2 \cdot 10^5 Hz) \times 3 * 10^{-9} s * 3(times) = 518 Hz$$

   - since one 1m^2 chamber contains 1250 virtual pads (320 kHz per chamber) , the final coincidence of the two chambers sandwiching the sMDT, gated at about 10 ns, produce a fake rate of:

$$(\sim 650 kHz)^2 \times 10^{-8} s \simeq 4.2 kHz$$

- This value can be further reduced by cutting in solid angle, accepting only the hit configuration corresponding to pointing tracklets. This function can be performed at the end of the trigger chain on all the proposed tracks, by means of a jump table
- Another background source arise from the low energy charged particles with an energy sufficient to trigger the first chamber. Even if small fraction of the total background is constituted by this type of events the fake rate increase substantially. For instance 1% of the background already corresponds to 1MHz/m^2 of triggers in the first chamber, which can coincide with a random hit on the second chamber. The strongest possible suppression of random hits is the best way to suppress also this type of background.

7.3 L1 trigger and electronics

1. **How the L1 signal are produced, starting from the detector signal till the formation of SL input**

   The combination of segments found by the mRPC and the EM TGCs will be very useful to reject uncorrelated backgrounds. Due to the excellent RPC time resolution every single hit can be selected on the base of a very strict space-time coincidence. The maximum selector electronic circuits that can determine the center of the clusters of fired strips is gated by this coincidence and deliver the hits to a segment trigger processor that performs the muon segment search. This segment trigger processor searches for coincidences with the predefined patterns of four strips in two doublets (equals to four single gas gaps) among the surviving hits. In particular these segments are required to roughly point to the IP not to be rejected, as shown in Fig. 34.The second coordinate coincidence is also required to reduce the amount of fake muons due to uncorrelated background hits and detector intrinsic noise. Another muon trigger processor receives the segments sent by the EM TGC trigger and combines them with the segments sent by the mRPC trigger. It performs a matching based on the proximity of the segments in the η and ϕ space. If the two segments are close, the angle difference is then used to determine the momentum of the muon passing through. If the segments are too far away from each other, the two segments will be thrown away and will not be considered to form a muon. Special attention needs to be given to the overlap region to avoid the same muon reconstructed twice. All successful fitted muons are sent to MUCIPi for further processing.

   The whole covered area is 35.4 m2 for small sectors and 43.7 m2 for big sectors, within a period of 25 ns, the average number of random hits expected for the whole covered area by the small wheel is about 200.

   Targeting Precise Signal timing
   The proposed design focuses on precise timing aided by differential measurements from both ends of the strips. A combination of these measurements provides exceptional signal timing via digital mean timers and a second coordinate is available from differential timing for background rejection purposes. The development of a second coordinate within a single layer eliminates ambiguities even at the highest rates. The precision of the second coordinate is far less than that available from the strips and is expected to be on order of a few centimeters. The second coordinate precision will be known from test on early version with the aid of off-line evaluation of the differential readout.

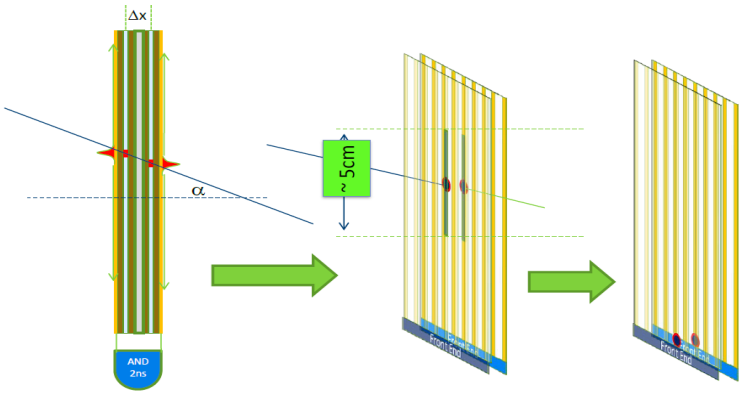

Figure 32: Benefit of using mean-timer electronics to determine the hit position along the phi strip. This will simplify the level 1 trigger algorithm and reduce random rate.

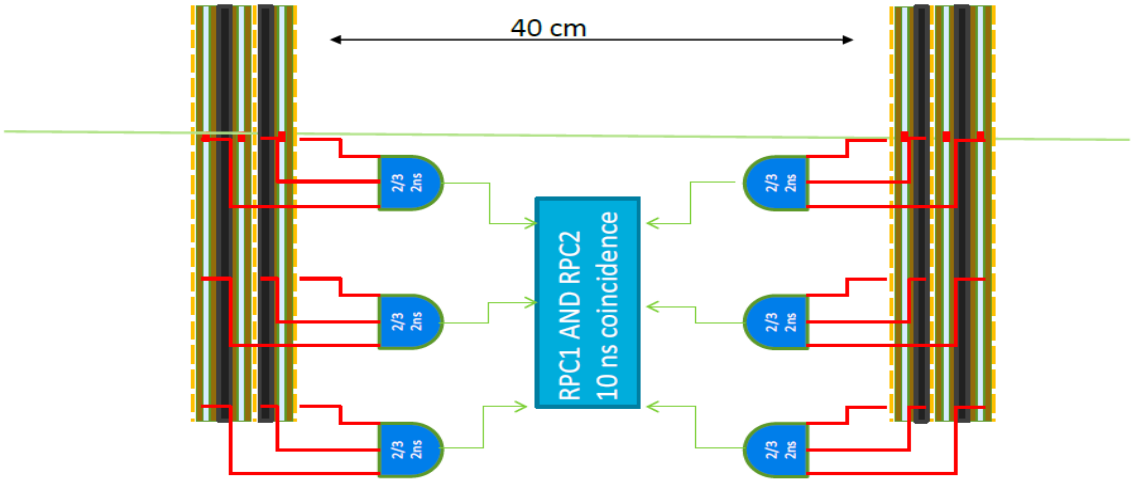

Figure 33: Layout of L1 trigger. The output from the maximum selector will be used to form the small wheel segments.

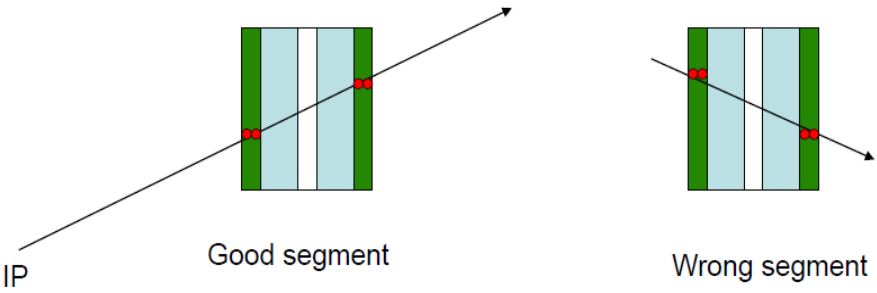

Figure 34: The segments determined by the new small wheel detector need to point to the IP. Segments that are not pointing to the IP will be rejected.

2. **Compatibility with Phase II upgrade**
   A small number of synchronous, 2 dimensional coincidence trigger segments from each azimuthal region would be natural to combine with the TGC trigger elements from the Big Wheel either at the existing trigger crates or at new crates located in USA-15. The results would be a confirmed high-Pt muon with a sharpened threshold.

3. **Latency**

The signal will arrive through the amplifier-shaper-discriminators and the digital-mean-timer a few tens nanoseconds after it is generated inside the detector. This takes in to account the arrival of signals from the most distant end of the strip and the cabling delays. A further delay of about 10 ns will be added by the coincidence requirements associated with the maximum selector. Thus, after a fixed delay < 100 with respect to the crossing, a two coordinate data unit is available. How many such units are to be processed in parallel awaits detailed simulations. One could imagine that a 2 out of 3 coincidence from 3 layers might be used on-chamber to reduce backgrounds by demanding pointing toward the IP, within appropriate cuts, to select high momentum and remove off angle tracks from a crude polar cut. A SW latency value consistent with the BW TGC should be easy to accomplish. Knowledge of the rejection of spurious hits will only be understood with detailed simulations.

Evaluation of the Trigger Scheme

We will make use of the ATLAS muon monitored drift tube (MDT) front-end readout electronics for testing the proposed mRPCs and the proposed trigger scheme. This test system can accept trigger and readout signals at MHz rates for burst periods to test the high rate capability of the detector. Certain modifications and developments are needed to get the signals from both ends the mRPCs. The readout is pictured in Fig. **??**.

In figure 35 the details of the electronics equipment of the η strip panel. On the side of the maximum selector, which reads out groups of 8 strips, one amplifier per strip is used. The maximum selector provides also the average charge of the strip group which is used by the meantimer. On the other end of the strip the analog sum of the same 8 channels is also amplified and delivered to the mean-timer. The cable length is adjusted within 100 ps tolerance.

Figure 35: η strip panel readout and space-time localization electronics.

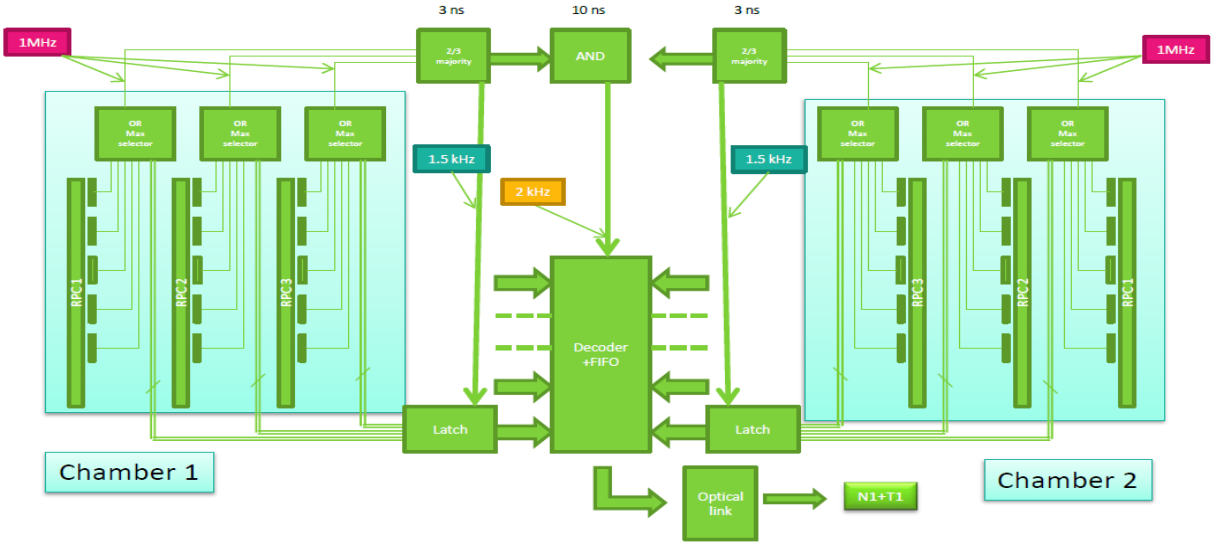

Figure 36: Layout of readout electronics.

- We will use offline computation of the differential timing from both ends to determine the hit position along the strip with a resolution of 5-10 cm.

- We will examine the need for an analog peak selector-digital encoder.
- We will compute the mean time of the signals read from both ends and examine the role of fast timing in the suppression of backgrounds. We will examine the suppression of combinatorial background using timing within a layer vs. multilayer timing.
- We will examine the precision in the bend direction to assess whether the proposed chamber can meet the ¡ 1 mr requirement with the level arms possible in the SW layout proposed.
- An optimal layout considering the number of layers, strip separation, coincidence timing, and circuit modularity will be examined.
- We will assess the background hit rejection of all algorithms considered.

7.4 Readout electronics and integration in DAQ

1. **Detailed description of electronics chain**

   The readout proposed for the data stream is to be shared with the MDT which requires a redesign of the mezzanine cards for higher density, higher serial readout rate, and repair of the pair modedifficulty. This also includes a redesign of the CSM to incorporate the GMT chip and up to date radiation hard electronics.

   If the goal of on-chamber multi-layer coincidence can be met, the large channel count electronics will be limited to the chamber level. For the trigger this would be arranged as synchronous fiber output of a small number of SW segments selected to be pointing toward the IP within a high momentum requirement in the polar angle and an appropriate match in azimuthal angle.

   For the data readout, hits need be stored in rather large level-1 buffers awaiting a trigger signal. For the MDT the readout window will be programmed to accept the full drift time as is now the case. For the mRPC the readout window can be quite small so readout rates will be smaller even with the large channel counts of the mRPC. Two modes of mRPC hit storage are likely, one that saves all hits and one that retains only hits that combine to form trigger segments. In a design that must include programmed timing alignment of signals from different layers for ns level timing, the first mode is necessary to tune the time alignment. A scheme of this kind was used in CDF where a custom IC (called the data phase chip) was included to provide time alignment of signals.

   With a mRPC with 1.25 mm strip repeat 2400 channels per meter signals leave both ends of the detector and converge at a front-end board where regional trigger primitives are generated. It is anticipated that a small number of selected segments will each leave this regional board on a synchronous (to the crossing) fibers. Data for readout upon a level-1 trigger will be stored on the regional board awaiting a level-1 trigger. This is similar to the current mezzanine and CSM design. Whether this mezzanine card equivalent sends its data to a shared CSM equivalent or an independent multiplexer is a design question. In either case the data format and design characteristic of the multiplexer are to be the same. Todays multi-conductor micro-coaxial cables are capable of 0.625 mm intervals.

The cable cross section to the regional board for both ends assuming 1mm packing of the 0.625 mm cables is 50 cm2/meter of detector width for all 3 layers of a 3 layer system. This appears to be quite doable. If the process of combining these signals into a small number of synchronous fibers for trigger and a small number of asynchronous fibers for readout, outgoing cable cross sections to the CSM equivalent will be small. A token passing scheme would permit the front-end cards to compact many channels into a single fiber for transmission to the multiplexer.

2. **Integration to DAQ**

3. **Readout related parameters, e.g. bandwidth requirements, number and granularity of read-out links**

4. **Compatibility with Phase II upgrade**

   This needs a decision of how the new MDT redesign of the mezzanines and CSM are changed. I think we should move to a token passing scheme for transmission between mezzanine cards (something the current AMT chip can do we do not use it). In such a scheme each mezzanine passes its request to send data to the next mezzanine with the last sending everyones data to a small fiber board for transmission to the CSM which can be far away if desired. Such a scheme lends itself to the mRPC which has many channels arriving at a single front-end board.

7.5 Services, infrastructure, and DCS

1. *Description of service scheme (including power system, read-out, trigger, alignment), cooling needs and other special requirements*

2. *Table with number of services (number of cables, outer diameter, cross section of leads)*

3. *Table with power consumption (per channel, chamber, total)*

4. *Required rack space*

   (a) *UX15 (include maximum allowed distance to detector if any)*

   (b) *US15 (power system)*

   (c) *USA15 (DAQ)*

5. *Gas system and distribution*
   Details on number of gas manifolds per sector (include drawings) and connections to chambers (serial, parallel?)). Size of pipes
   Required nominal, minimum, and maximum flow
   Required precision of gas mixture
   Safety measures in case of inflammable gas
   Required rack space for gas system in SGX1, USA15, UX15

6. *Integration in DCS system, requirements for DCS*

Cable	Number of cables (granularity)	Outer cable diam. (mm)	Cross section of leads (mm^2))
HV			
LV			
Monitoring and control			
Front-end links			
Calibration			
Alignment			
Miscellaneous			

Table 12: Example table number of services per chamber

Chamber	Number of channels	Power consumption per channel	Total power consumption

Table 13: Example table: Number and types of chambers per sector

8 Detector concept 3 : Micromegas (working title)

Introduction to this concept.

This section should describe the technology concept, details up to the level of a single chamber should be given in the appropriate appendix.

8.1 Detector technology and layout

1. *Description of detector concept (a detailed description of the working principle of each detector should be given as an appendix).*
   If more than 1 technology is used motivate the decision and detail how they work together (e.g. can services be shared, is the information of the trigger chambers used in the precision chambers, how are combined chambers assembled etc.)

2. *List of all operating parameters*

3. *Detailed layout: acceptance, description of chamber overlap and dead areas, drawings*

4. *Tables with chambers sizes, number of channels*

5. *Internal alignment scheme (the overall common endcap alignment scheme is described in the previous chapter)*

6. *Calculations about mechanical stability and expected deformations due to gravity, temperature changes, (magnetic field) etc.*

7. *Requirements for mount points*

8. *Details of service points and other positions where access is needed*

9. *Concept for chamber replacement (what needs to be dismounted etc.)*

Micromega/TGC/RPC/MDT	Type 1	Type 2
Number of chambers		
Radial extension (mm)		
Minimum length in ϕ (mm)		
Maximum length in ϕ (mm)		
Thickness in z (mm)		
Mass (kg)		
Number of layers		
Number of channels		

Table 14: Example table chamber types

Chamber	Small sector	Large sector

Table 15: Example table: Number and types of chambers per sector

8.2 Performance

Summary of chamber performance, details in appendix of technology.

1. *Spatial and angular resolution as functions of rate and angle of incidence*
2. *Time resolution*
3. *Efficiency (single measurement and segment)*
4. *Double track resolution*
5. *Rejection of fake and background tracks*

8.3 L1 trigger and electronics

1. *How the L1 signal are produced, starting from the detector signal till the formation of SL input.*
2. *Latency (calculation, measurement with demonstrator)*
3. *Compatibility with Phase II upgrade*

8.4 Readout electronics and integration in DAQ

1. *Detailed description of electronics chain*
2. *Integration to DAQ*
3. *Readout related parameters, e.g. bandwidth requirements, number and granularity of read-out links*
4. *Compatibility with Phase II upgrade*

8.5 Services, infrastructure, and DCS

1. *Description of service scheme (including power system, read-out, trigger, alignment), cooling needs and other special requirements*
2. *Table with number of services (number of cables, outer diameter, cross section of leads)*
3. *Table with power consumption (per channel, chamber, total)*

4. *Required rack space*
   (a) *UX15 (include maximum allowed distance to detector if any)*
   (b) *US15 (power system)*
   (c) *USA15 (DAQ)*
5. *Gas system and distribution*
   Details on number of gas manifolds per sector (include drawings) and connections to chambers (serial, parallel?)). Size of pipes
   Required nominal, minimum, and maximum flow
   Required precision of gas mixture
   Safety measures in case of inflammable gas
   Required rack space for gas system in SGX1, USA15, UX15
6. *Integration in DCS system, requirements for DCS*

Cable	Number of cables (granularity)	Outer cable diam. (mm)	Cross section of leads (mm^2))
HV			
LV			
Monitoring and control			
Front-end links			
Calibration			
Alignment			
Miscellaneous			

Table 16: Example table number of services per chamber

Chamber	Number of channels	Power consumption per channel	Total power consumption

Table 17: Example table: Number and types of chambers per sector

9 Expected muon performance with NSW [SV]

Discussion of overall performance. L1 trigger, muon reconstruction, efficiency, fake, sensitivity to a few layout parameters (number of layers, ...),

10 Integration, assembly and commmissioning [JD]

11 Cost, resources and schedule [LP, TK]

12 Conclusions

Appendices

A Radiation background

Discussion of expected cavern background and its uncertainty based on simulations and measurements with muon detectors, and finally give a reference figures and safety factor.

- *Overview of cavern background. It's nature, origin, shielding strategy*
- *Simulation result. R distribution in the small wheel region. 14 TeV, Al beam pipe, 14 TeV steel beam pipe, 7 TeV steel beam pipe.*
- *Measuremenents with pp collision. MDT, CSC*
- *Summary figure. Reference figures.*

A.1 simulation

B Small tube

Detail of detector technologies proposed for use in the small wheel detector, including the status of developments. Include a description on the status and size of available prototype chambers.

This section should describe the technology up to the level of a single chamber.

B.1 Assembly

Describe the assembly procedure. Include details on

1. *Achieved mechanical precision of signal generating parts (i.e. strips or wires)*
2. *Speed of assembly*
3. *Splitting of work and logistics between production site*

B.2 Quality Assurance and Commissioning

1. *Quality assurance of all individual chamber parts, include necessary manpower and rate of tests*
2. *Quality assurance and commissioning scheme of full chambers, include necessary manpower and rate of tests*
3. *How can/is data of the commissioning used later (e.g. strip or wire positions)?*

Note: A common commissioning strategy during and after assembly of the wheels will be given in a previous chapter

B.3 Operation, Maintenance and Safety

Describe in detail the impact of failures of single components (gas leak, HV breakdown, front-end electronics) on the detector operation. Comment on possible built-in redundancy.

Describe in detail the possible scenarios for maintenance on the detector and the exchange or repair of detector parts.

Describe the risks associated with the technology during operation and maintenance (HV, maximum currents, flammable gas etc.)

B.4 Performance

Describe in detail the performance of the detector, including results from test beam studies. Include studies with background radiation (γ, n, p)

1. *Detector occupancy as function of rate*
2. *Spatial and angular resolution as functions of rate and angle of incidence for single point measurements and segments*
3. *Time resolution*
4. *Efficiency (single measurement and segment)*
5. *Double track resolution*
6. *Rejection of fake and background tracks*
7. *Sensitivity to background radiation*
8. *Performance limits (maximum rate)*

B.5 Aging Tests

Describe in detail results from aging tests for all components, the detector itself including the on-chamber gas distribution, read-out and/or trigger, alignment, and detector control electronics.

B.6 Cost, Funding, and Manpower

1. *Table of cost of each component, full chambers and total*
2. *Additional costs (e.g. integrating two technologies)*
3. *Arrangements for funding (if any so far)*
4. *List of manpower needs, especially include statements on the the current and future availability of experts (for at least the full construction and commissioning period, i.e. 2012 – 2019, better also for the operation)*

C TGC

D RPC

E Micromegas

References

[1] G. Aad et al. Expected Performance of the ATLAS Experiment - Detector, Trigger and Physics. 2009.

[2] G. Aad et al. The ATLAS Experiment at the CERN Large Hadron Collider. *JINST*, 3:S08003, 2008.